Design, control, and visual navigation of the DelftaCopter VTOL tail-sitter UAV

de Wagter, Christophe; Ruijsink, Rick; Smeur, Ewoud; van Hecke, Kevin; van Tienen, Freek; van der Horst, Erik; Remes, Bart

DOI
10.1002/rob.21789

Publication date
2018

Document Version
Final published version

Published in
Journal of Field Robotics

Citation (APA)
de Wagter, C., Ruijsink, R., Smeur, E., van Hecke, K., van Tienen, F., van der Horst, E., & Remes, B. (2018). Design, control, and visual navigation of the DelftaCopter VTOL tail-sitter UAV. *Journal of Field Robotics*, *35*(6), 937-960. https://doi.org/10.1002/rob.21789

Received: 2 March 2017 | Revised: 12 January 2018 | Accepted: 26 February 2018

DOI: 10.1002/rob.21789

REGULAR ARTICLE

WILEY

Design, control, and visual navigation of the *DelftaCopter* VTOL tail-sitter UAV

Christophe De Wagter | **Rick Ruijsink** | **Ewoud J. J. Smeur** | **Kevin G. van Hecke** | **Freek van Tienen** | **Erik van der Horst** | **Bart D. W. Remes**

Micro Air Vehicle Lab, Delft University of Technology, Delft, The Netherlands

Correspondence
Christophe De Wagter, Micro Air Vehicle Lab, Delft University of Technology, Kluyverweg 1, 2629HS Delft, The Netherlands.
Email: c.dewagter@tudelft.nl

Abstract

To participate in the *Outback Medical Express UAV Challenge 2016*, a vehicle was designed and tested that can autonomously hover precisely, takeoff and land vertically, fly fast forward efficiently, and use computer vision to locate a person and a suitable landing location. The vehicle is a novel hybrid tail-sitter combining a delta-shaped biplane fixed-wing and a conventional helicopter rotor. The rotor and wing are mounted perpendicularly to each other,and the entire vehicle pitches down to transition from hover to fast forward flight where the rotor serves as propulsion. To deliver sufficient thrust in hover while still being efficient in fast forward flight, a custom rotor system was designed. The theoretical design was validated with energy measurements, wind tunnel tests, and application in real-world missions. A rotor-head and corresponding control algorithm were developed to allow transitioning flight with the nonconventional rotor dynamics that are caused by the fuselage rotor interaction. Dedicated electronics were designed that meet vehicle needs and comply with regulations to allow safe flight beyond visual line of sight. Vision-based search and guidance algorithms running on a stereo-vision fish-eye camera were developed and tested to locate a person in cluttered terrain never seen before. Flight tests and a competition participation illustrate the applicability of the *DelftaCopter* concept.

KEYWORDS

aerial robotics, control, emergency response, perception, sensors

1 | INTRODUCTION

The possible applications of aircraft with combined efficient long-range flight and hovering capabilities are numerous. Typical examples are operation from ships, over vast forests or departing from densely built-up areas. Unfortunately, requirements for fast and slow or even hovering flight are very contradictory (Anderson, 1999), making it difficult to design an aircraft that is efficient and controllable while having a very large flight envelope.

Though hybrid aircraft have existed for a long time (Anderson, 1981), the first hybrid aircraft had to carry a human pilot. This created some additional constraints, as the pilot needs to be comfortable and able to see the surroundings at all times. Early manned designs often included complex and heavy mechanisms to tilt the wing and motors during transition from hover to forward flight (Rosenstein & Clark, 1986), such that the pilot can remain vertical. Similar tilt-wing concepts have also been tried in unmanned air vehicles (UAV), but the concept remains heavy and has complex aerodynamic and control properties (Çetinsoy et al., 2012; Schütt, Hartmann, & Moormann, 2014).

With the advent of UAV, several hybrid aircraft concepts that were previously impracticable have gained new interest. This includes the so-called tail-sitter UAV. The first hybrid tail-sitters were combinations of fixed-pitch quad-rotor helicopters with a flying wing such as the Quadshot (Smeur et al., 2014). These types of platforms had four propellers and typically two aerodynamic actuators for forward flight. Oosedo et al. (2013) tried several structural variations with good results, but the fixed-pitch propellers make it theoretically impossible to be very efficient in both hovering and forward flight.

To address this problem, the ATMOS-UAV* platform (De Wagter, Dokter, de Croon, & Remes, 2013) used two sets of propellers with different pitch. Large low-pitch propellers are used during hover, whereas small high-pitch propellers are better suited for fast forward flight (Hulsman, De Groot, & Dokter, 2014). The large main hovering propellers fold during forward flight. Using two types of propellers makes the yaw control by torque variation impossible. Yaw control was therefore done by aerodynamic actuators on the wing which have very low effectiveness during hover. Later versions tried to rotate the tip motors to gain better yaw control, but this comes at the cost of a lot of added structural weight.

To reduce the number of moving parts and actuators and hereby reduce complexity and system weight, several researchers have investigated a tail-sitter concept with only two motors and two aerodynamic actuators. Bapst, Ritz, Meier, and Pollefeys (2015) have added two hover motors to an existing delta wing. With little added weight, they showed that the delta wing, which was efficient in forward flight, could also hover, albeit with low control authority and disturbance rejection when compared to the quadrotor-based tail-sitters. Verling et al. (2016) have designed a dedicated platform with larger motors and a smaller wing, which increases the control authority in hover at the expense of forward flight efficiency. To be able to use a better wing, Ke, Wang, and Chen (2016) proposed a concept with a tail section with an elevator. Phung and Morin (2013) analytically found propeller orientations with respect to the main wing that resulted in more efficient forward flight, but did not show flight results. Although lighter and simpler than the four motor concepts, the two motor concepts still suffer from the fixed pitch propellers that cannot be efficient both during hover and fast forward flight. To address this problem, Wong, Guerrero, Lara, and Lozano (2007) created a version with variable pitch. This theoretically makes it possible to achieve more efficient forward flight but comes at the expense of two extra actuators to control the pitch and added weight from the mechanisms.

All versions of the dual mot\or tail-sitter use aerodynamic actuators, which have a control effectiveness that is very dependent on the airspeed of the vehicle. The effectiveness depends on the amount of air that passes over the aerodynamic surfaces. In hover, only the downwash from the propellers passes over the control surfaces. This creates relatively small moments compared to the moments induced by turbulence on the entire wing. In fast forward flight, the control surfaces become very sensitive due to the large amount of air that passes over them and this requires the controller to use a very wide range of gains depending on speed. In case of fast descend during hover, with air flowing in reverse direction over the wing, there is even a point where the platform becomes uncontrollable, when this reversed flow from the descend cancels out the downward flow of the propellers (Itasse, Moschetta, Ameho, & Carr, 2011a; Itasse, Moschetta, Carr, & Ameho, 2011b).

Further reducing the number of heavy motors, other concepts reduced the number of propellers to one and use at least three aerodynamic actuators. Knoebel and McLain (2008) use a delta wing with a single fixed-pitch propeller up front and is able to hover. The single propeller creates a torque that must be compensated with aerodynamic actuators, reducing the maximum perturbation they can handle. Matsumoto et al. (2010) proposed a similar setup but based on a conventional aircraft with a main wing and a tail. To solve the torque problem of the single propeller, Escareno, Stone, Sanchez, and Lozano (2007) proposed a coaxial dual propeller version, which also results in slightly higher efficiency at the cost of an extra motor and coaxial system (Escareno, Sanchez, Garcia, & Lozano, 2008). Although all three concepts can be made very efficient in forward flight, they suffer from all effects described above due to their fixed-pitch propellers and aerodynamic control surfaces. This limits their ability to handle strong turbulence while hovering.

Conventional helicopters not only vary the pitch of the main rotor for all blades collectively, but they can also create different lift on two opposing blades. This is referred to as cyclic control, as the pitch is increased or decreased every time the blade passes a certain point in its cycle. This control of blade pitch is done through a conventional helicopter rotorhea plate. While this adds complexity and maintenance, it allows the rotor to very quickly create very large control moments that, unlike aerodynamic actuators, are nearly independent on vehicle flight speed (Bramwell, Balmford, & Done, 2001). Moreover, propulsion theory predicts that the best efficiency is obtained with a single rotor that accelerates a lot of air a little bit (Roskam & Lan, 1997). To solve the combined requirement on control authority and efficiency, a new concept is proposed. By combining a large efficient conventional helicopter rotor with cyclic control and a pair of delta wings, a platform is obtained that can hover efficiently, fly forward efficiently, and still maintain very good control in case of perturbations during hover.

1.1 | Medical express challenge

A use-case for vertical takeoff and landing (VTOL) aircraft with long-range capabilities is the Outback Medical Express UAV Challenge 2016. The Outback UAV Challenge has a long history of creating realistic but very hard challenges for teams to improve the state of the art (Boura, Hajicek, & Semke, 2011; Erdos & Watkins, 2008; Erdos, Erdos, & Watkins, 2013).

The 2016 edition of the Outback UAV Challenge was called *Medical Express* and had set its competition goals to stimulate the development of aircraft with both hovering and long-range flight capabilities. The competition requires an unmanned vehicle to take off from a model airstrip in *Dalby, Australia* and fly to a remote location 30 km away. The selected remote area had often been inaccessible due to floods for real. At the location, a lost bush walker must be located. The unmanned vehicle must then select a suitable landing location within 80 me from the found person, but for safety reasons may never come closer than 30 m to the person (Clothier, Williams, & Fulton, 2015). After an automatic vertical landing, medical assistance is delivered before flying back to base with a medical sample.

1.2 | Long-distance VTOL

This paper proposes a novel UAV design (see Figure 1) that combines efficient and high control authority hover with efficient long-range

---

* ATMOS: Autonomous Transitioning Multi-rotor Observation System.

FIGURE 1 Novel hybrid UAV, which combines a cyclic and collective pitch controlled main rotor with a biplane delta wing and torque compensating tip rotors. The biplane concept adds structural rigidity and minimizes the lateral surface area to reduce the perturbations from turbulence during hover. The large main rotor allows efficient hovering flight, whereas the cyclic control provides large control authority in hover

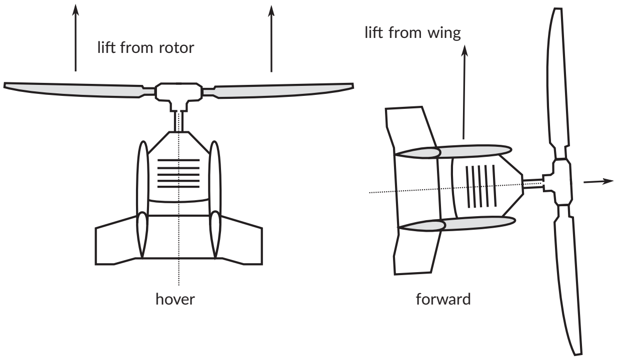

FIGURE 2 Lift generation in hover and forward flight

fast flight. While the design was optimized for the Outback Medical Express, it has applications far beyond. It contains all avionics and computer vision needed to turn it into a flying fully autonomous vision guided robot. During hover, all lift is provided by the main rotor and it uses tip rotors and ailerons to compensate for the main rotor torque. During forward flight, it pitches down almost 90° and transitions to a fixed-wing aircraft with a large propeller, as illustrated in Figure 2.

In hover, the *DelftaCopter* is basically a helicopter. In forward flight, the motor rpm is reduced and the rotor blade pitch is increased to reach flight speeds of around 20–25 m/s. These flight speeds are necessary to cover the required 60 km in under 1 h, even in case of winds up to 25 kt.

The delta wing of the *DelftaCopter* has the advantage of being simple and compact. Not needing a long fuselage and tail section also yields advantages in the landing phases. Natural wind has a severe wind gradient close to the ground (Thornthwaite and Kaser, 1943). When hovering, the top of the aircraft experiences a higher wind velocity than the lower part which calls for aircraft without a long tail.

The choice for a biplane was made on three grounds:

- Two wings have less surface area exposed to the wind in VTOL mode, compared to a single wing that can provide the same lift. This diminishes the perturbations of takeoff and landing in wind.
- The two wings and fins at the tips form a box construction with landing legs at the extremities. This results in a large footprint and thereby maximal stability when landed.
- A biplane configuration remains nonstalled in a higher range of angles of attack (Olson and Selberg, 1976), which gives advantages in the transition from hover to forward flight and back.

1.3 | Outline

The outline of the paper is as follows. First, a propulsion system for both hover and forward flight is derived in Section 2. Then the energy consumption (Section 3) is addressed. Based on the available propulsion and energy, the aerodynamic and structural design are detailed in Section 4. Wind tunnel measurements are analyzed in Section 5. The electrical design is explained in Section 6. The control of the *DelftaCopter* is explained in Sections 7 and 8. An overview of the on-board computer vision follows in Section 9. Flight testing is described in Section 10, and finally the conclusions and recommendations follow in Sections 11 and 12.

2 | PROPULSION DESIGN

The design of a propulsion system that is efficient in the wide range from fast forward flight down to stationary hovering flight is always a challenge. For the *DelftaCopter*, the propulsion is designed to be a compromise between efficient hover and efficient forward flight. This results in a rotor blade that is significantly different from rotors seen in conventional helicopters.

The maximum efficiency for hover is obtained using a single large rotor with low pitch angle (Bramwell et al., 2001). Also for forward flight, a single rotor is the most efficient solution but a higher pitch angle is required (Anderson, 1999). While in theory a single blade rotor is more efficient than a two blade rotor, in practice to balance vibrations at all power settings, the dual blade is more practicable than a single blade.

Blade twist is the change in angle of attack between tip and root. Since the tip of a propeller or rotor moves a lot faster than the root, it needs a different angle of attack to be optimal. The *DelftaCopter* rotor blades are designed with significant twist, yielding a substantial performance increase over a rotor-blade without twist.

Conventional helicopters suffer from twist, as in fast forward flight the rotor undergoes a lot of airflow not in the direction of the rotor axis but from the side. This lateral flow hits both tip and root of the blades at the same speed, hereby changing the optimal blade angles and reducing efficiency in case of twist. In the *DelftaCopter*, the use of twist is possible thanks to the transitioning as the rotor can always be kept in an axial flow regime.

2.1 | Propeller design

For efficient hovering, the diameter has to be big enough to reach a reasonable figure of merit (Bramwell et al., 2001). For forward flight where the power is significantly less than for hover, the big diameter is

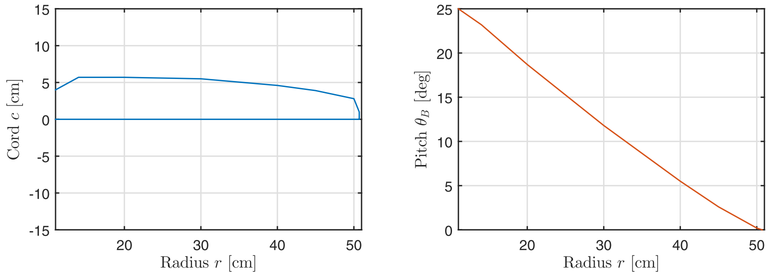

FIGURE 3 Blade cord $c(r)$ and blade pitch angle $\theta_B(r)$ of the designed rotor blade in function of the radial location r

TABLE 1 Airfoil cord $c(r)$ and pitch angle $\theta_B(r)$ at given radius r

r (cm)	c (cm)	θ_0 (°)
11	4	25.0
14	5.7	23.2
20	5.7	18.7
30	5.5	11.8
40	4.6	5.5
45	3.9	2.6
50	2.8	0.2
50.7	1.0	0

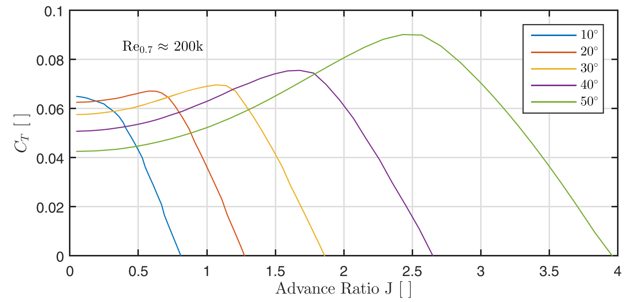

FIGURE 4 The thrust coefficient C_T or dimensionless thrust in function of advance ratio J. Low advance ratios correspond to low airspeed and high rpm, which typically occur in hover, whereas high advance ratios correspond to high airspeed with lower rpm. Note that for higher pitch angles of the propeller blades, the propeller can only deliver its maximum thrust if advancing sufficiently while it turns. Also note that advance ratios over 1.5 are considered very large. The *DelftaCopter* blades can still produce thrust at very high pitch angles

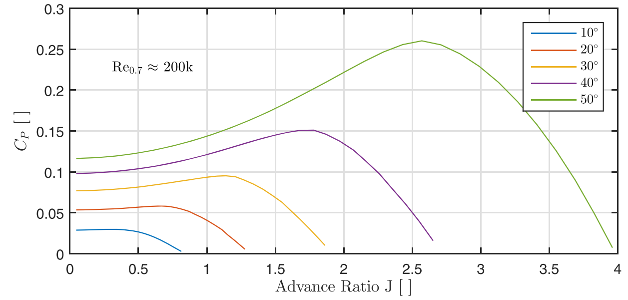

FIGURE 5 Propulsion power coefficient C_P shows the dimensionless power required in function of advance ratio J. While higher advance ratios can be obtained at higher pitch angles, it takes more power to reach the same rpm

acceptable when the rpm is reduced and the pitch is increased (Roskam & Lan, 1997). The *DelftaCopter* therefore uses a large rotor to hover efficiently and create large control moments and increases the pitch in forward flight.

The design of the propeller was iteratively performed with the support of *PropCalc 3.0*† (Schenk, 2007). The design iterations minimized both hover power and forward flight power for a given weight of the *DelftaCopter*. Diameter, blade twist, radius, and airfoils were varied as inputs, and the corresponding power at the required lift was computed and iteratively minimized. A diameter of 1 m was finally selected as a compromise between hover and forward flight requirements. A blade twist of 25° from root to tip was applied. For the airfoil, the *MA409* section was chosen being targeted at a *Reynolds* numbers of $Re_{0.7}$ = 200.000 and below.

The resulting propeller is shown in Figure 3, and the size is given in Table 1. Figure 4 shows the thrust coefficient C_T of this propeller in function of the nondimensional advance ratio

$$J = \frac{V_a}{(n \cdot D)} \tag{1}$$

where n is the propeller rotational speed in rotations per second, D the diameter, and V_a the inflowing free stream air velocity perpendicular to the propeller plane. The advance ratio is a useful nondimensional velocity in propeller theory, since propellers and rotors will experience the same angle of attack on every blade airfoil section at the same advance ratio regardless of actual forward speed (Glauert, 1935). The thrust coefficient C_T, the power coefficient C_P (Figure 5), and the efficiency in Figure 6 are computed as

$$C_T = \frac{T}{\rho \cdot n^2 \cdot D^4} \tag{2}$$

$$C_P = \frac{T}{\rho \cdot n^3 \cdot D^5} \tag{3}$$

$$\eta = \frac{V_a}{n \cdot D} \cdot \frac{C_T}{C_P} \tag{4}$$

where ρ is the air density and T is the thrust.

---

† See http://www.drivecalc.de/PropCalc/

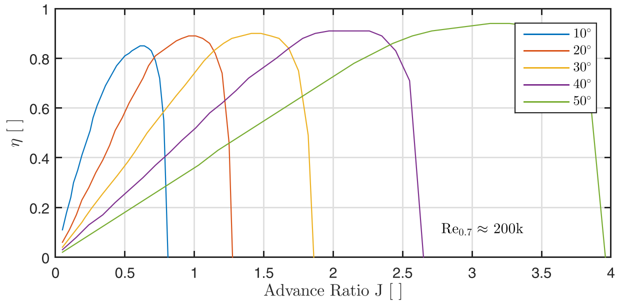

FIGURE 6 The propulsion efficiency in function of advance ratio clearly shows low pitch angles are needed at low advance ratios and larger pitch angles at larger advance ratios. In other words, propellers with large blade pitch must travel further through the air for each rotation to be efficients

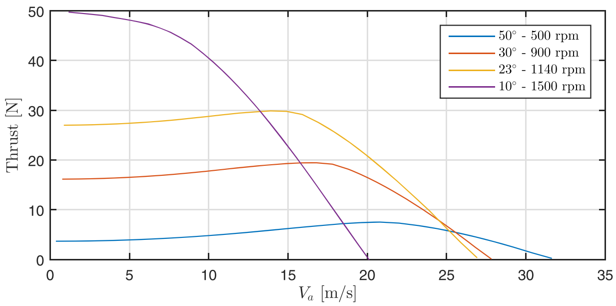

FIGURE 7 Propulsion thrust T in function of the incoming free stream airspeed V_a at selected pitch angles and rpm. Low V_a corresponds to hovering flight, whereas high V_a corresponds to cruising flight. In hover, all the weight of the *DelftaCopter* (≈ 43 N) must be carried by the rotor. This can only be done at low pitch angles and an rpm of 1500. On the other hand, at low pitch angles the *DelftaCopter* would never be able reach 20 m/s as the thrust becomes zero at that speed. Meanwhile, using very high pitch angles of 50°, thrust can be generated up to at least 30 m/s

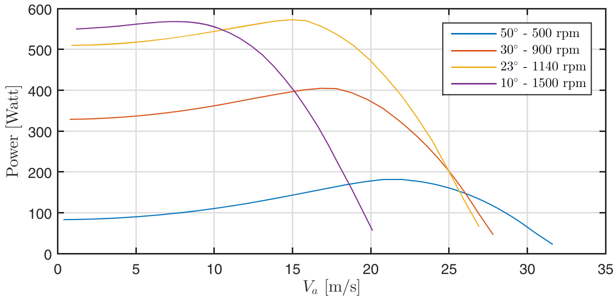

FIGURE 8 Available propulsion power at selected pitch angles and rpm. The lower V_a corresponds to hover, whereas the higher V_a corresponds to fast forward flight. Note that propulsion efficiency and motor efficiency must be added before the actual power used is found

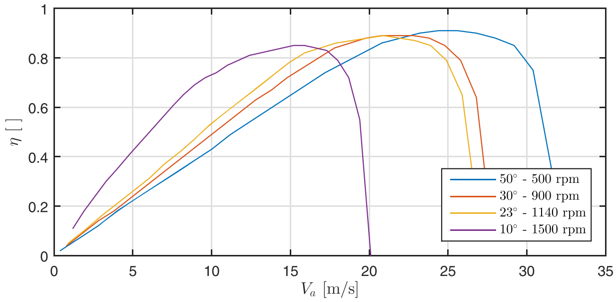

FIGURE 9 Propulsion efficiency defined as power obtained divided by power applied at selected pitch angles and rpm in function of airspeed. This shows the most efficient pitch setting in function of airspeed V_a. Up to airspeeds V_a of about 16 m/s, the most efficient pitch setting is 10°. For a speed of 20 m/s, the pitch setting of 10° is not possible anymore but ≈ 23° seems quite efficient. The pitch setting of 50° only becomes more efficient than 30° at speeds over 23 m/s

Figure 7 converts the dimensionless blade properties into actual scaled thrust T that the designed propeller will achieve in function of the incoming airflow V_a for various collective pitch and rpm settings of the blades. Higher thrust for hover or forward acceleration can only be obtained at higher rpm. Lower airspeeds V_a correspond to hovering conditions or slow vertical climb as a low V_a means the rotor moves little compared to the air. Higher V_a occur in fast forward flight. The required shaft power P to achieve this thrust is shown in Figure 8. Finally, Figure 9 shows the efficiency η of the total designed propeller.

This rotor is achieving sufficient required hover thrust (see Figure 7) at 1500 rpm with 10° tip pitch angle. For very fast forward flight, the best efficiency at 25 m/s (see Figure 9) is obtained using 500 rpm with 50° tip pitch angle. The propeller would then produce about 5.5 N thrust.

During the wind tunnel measurements (see Section 5) and flight tests (see Section 10), the drag of the *DelftaCopter* was found to be higher than estimated in the concept phase. To overcome this higher drag, a higher thrust was needed, which could only be obtained (see Figure 7) by using a lower pitch and increased rpm. While this results in a slightly lower maximal forward cruise speed, it also has advantages as it improves the control responsiveness and allows to climb more quickly when required. According to the propulsion design above, for forward flight at slightly lower cruise speeds of ≈ 21 m/s the most efficient setting is a pitch angle of about 23° combined with a reduced rpm of about 1,140 rpm.

2.2 | Motor

Once the propeller design was shown to yield good efficiency in both flight regimes, a corresponding motor was chosen capable of delivering the required torque and power. A 105-kV direct-drive sensorless brushless direct current motor was selected. An *iPower MT8017* motor rated for 900 W and 40 A was used and powered at a nominal voltage of 22.2 V from the six cell lithium-polymer pack. This 90-mm diameter outrunner weighs 385 g and was able to spin the 1-m diameter rotor at 1650 rpm in hover at full load. A higher torque motor able to achieve the same rpm would have been preferred but was not available at the moment of the design.

2.3 | Silent

The absence of gears in the direct drive system with a lower rpm motor directly on a large efficient low rpm main rotor reduces the three main sources of sound. In hover, the *DelftaCopter* produces noise equivalent to a medium-sized quadrotor like a DJI Phantom, with most noise originating from the high rpm fixed pitch tip propellers. But when transitioning to forward flight, the tip propellers are shut off completely and the main rotor rpm is reduced,which causes the *DelftaCopter* to become very silent. This reduced noise production is considered to be a significant benefit of using one large efficient rotor with low disk loading, low rpm, and a direct drive motor.

3 | ENERGY SUBSYSTEM DESIGN

Common battery technologies for electric UAV are lithium-polymer and lithium-ion batteries. Even higher energy densities can be achieved using fuel cells (Larminie, Dicks, & McDonald, 2003). But because of the short mission time of less than 1 h and high flight speed involved in the competition, the power these systems can deliver is also important. No fuel cells could be found within the weight budget and power rating, but instead lithium cells were used.

The choice between the more energy dense lithium-ion and higher current rated lithium-polymer types is not obvious. Two cells were found that in theory should have sufficient energy to fly the mission; namely the 3300 mAh *LG-HG2-3300* lithium-ion battery and the 2700 mAh *Extron 2700* lithium-polymer battery. While the former has 22% more energy, it becomes very inefficient at loads close to or over 3.3 A (1C).

Moreover, while battery data sheets contain information on discharge characteristics under constant load, batteries can behave differently under varying loads. To test which battery was actually able to deliver the required power for the foreseen mission, a battery test setup was constructed,which applied a load that simulates an actual flight while the battery voltage and the current are logged.

An energy profile was computed from the mission requirements. It consists of a so-called *high-load phase* during vertical takeoff, followed by an endurance *low-load phase* during the cruise and another *high-load phase* during the landing. After a short down time, there is also a return flight with the same profile.

DelftaCopter needs six lithium cells in series to boost the voltage to the required 22.2 V nominal as single lithium cells have a nominal voltage of 3.7 V. Three series of cells are then placed in parallel to increase the maximal allowed discharge current and be able to deliver the required peaks of 600 W in climb. This results in a total of 18 cells. All battery testing is done on a single cell. Current during hover was computed to be about 7.5 A per cell and is further referred to as the *high-load* while during forward flight the current per cell is about 2.5 A, which is referred to as the *low load* (see Figure 10).

Figure 11 shows the laboratory battery discharge test results for the best lithium-polymer and best lithium-ion battery for the *DelftaCopter*. Large differences can be observed in the discharge voltage while both are loaded with the same current. It can be seen that the voltage of the lithium-ion cell reaches critically low levels of 2.7 V before the end of the flight. While the lithium-ion cells contains 22% more mAh under ideal conditions, namely 3300 mAh compared to 2700 for the lithium-polymer cell, under the mission load its delivers less energy. In the end the *LG-HG2-3300* could not deliver the power needed for the final landing. The *Extron 2700* lithium-polymer cells were selected for the *DelftaCopter* as they could better cope with the high loads of the hover and the fast discharge rate imposed by the relatively short competition time.

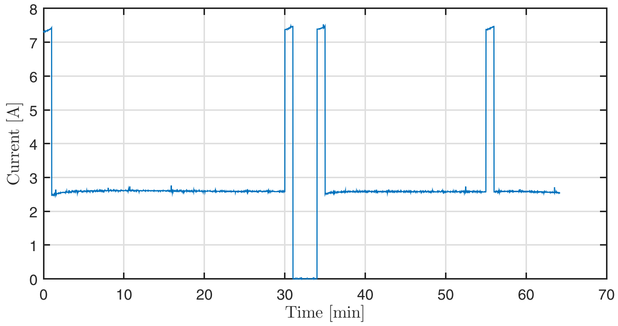

FIGURE 10 *Battery discharge test*: Discharge current in function of time using a programmable dummy load. The load applied to a test battery emulates the load the cell would have during the competition and emulates a 1-min hovering takeoff, followed by an efficient 29 min forward cruising flight, a 1-min hovering landing, 3 min of waiting time, and the same return flight. The current in this figure correspond to a single cell, whereas the actual *DelftaCopter* uses three cells in parallel and can deliver three times more current

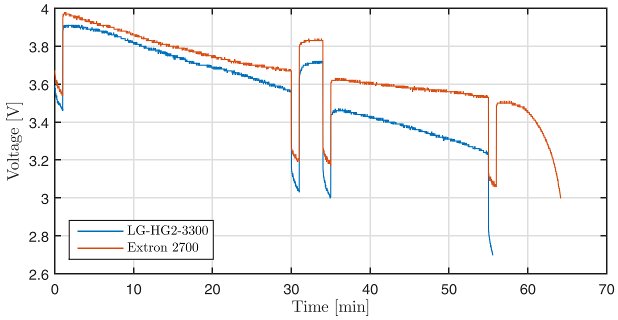

FIGURE 11 *Battery discharge test*: Voltage in function of time for a single lithium-polymer versus lithium-ion battery subjected to the mission load profile. *DelftaCopter* uses six cells in series to boost the voltage to 22.2 V nominal. Although the *LG-HG2-3300* has 22% more mAh than the *Extron 2700*, under the load of the *DelftaCopter* mission it is the first to be depleted due to the high discharge rate

4 | AIRFRAME DESIGN

Given the propulsion system, energy package, and performance requirements, a fixed-wing airframe was designed. The airframe needs to generate lift during fast forward flight with little drag, but at the same time it must also accommodate all the systems of the flying robot, including a swash-plate system for the control of the main rotors blades. Finally, it must provide structural integrity for the airframe to land as a rotorcraft.

4.1 | Structural

When the *DelftaCopter* is in hover, the wings acts as a landing gear but also make the helicopter more sensitive to lateral gusts. The biplane configuration has the advantage that the total lateral surface area in

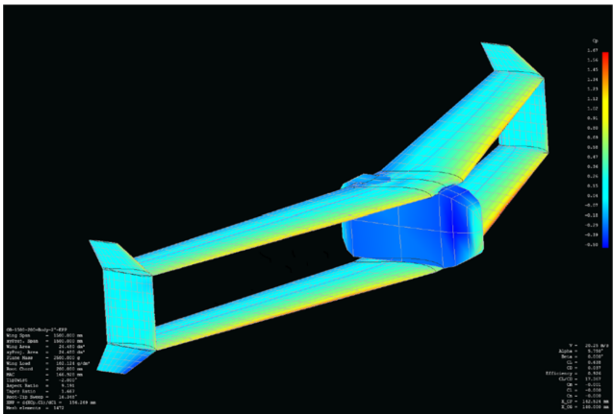

FIGURE 12 Screenshot from XFLR drag computations. The biplane wings and wing tips as well as the fuselage are modeled. The color shading reflects the pressure coefficient C_P

hover is significantly reduced, compared to a single wing. This means its size and corresponding moments are reduced, while at the same time the two wings also provide a stable rectangular basis for landing. The wings are kept together by a central assembly that also contains the rotor. Based on the blade size, parts from a rotor-head and swash-plate system from a *LOGO480*[‡] were used and built into an own carbon–aluminum frame. The rotor head was equipped with shorter blade grid handles to achieve a higher range of pitch angles.

4.2 | Aerodynamic design

A delta-shaped auto-stable flying wing concept was selected. This removes the need for a vertical stabilizer and fits well behind the main rotor. A "Peter Wick" *PW51*[§] airfoil was manually selected. It has some reflex making it marginally stable. The *PW51* is an airfoil designed for and proven in flying wings at Reynolds numbers from 100, 000 till 800, 000. The pitching moment is rather low to around zero. The airfoil has a good behavior at low angles of attack required for a high-speed cruise, whereas a $C_{L_{\max}}$ of around 1.2 is still good for a reflex airfoil of these proportions. The thickness of 8.9% is enough to allow a carbon-free construction. Finally, it has good stall properties, which is important during the transitioning phase. Passive longitudinal stability in forward flight is achieved when the delta wing is given 18° of sweepback and 1° washout. The wingspan is set at 1.5 m, and the cord decreases from 20 cm at the root to 12 cm at the tip. Lift and drag computations were performed using XFLR (Drela, Youngren, Scherrer, & Deperrois, 2012). Figure 12 shows a view from the three-dimensional model.

Figure 13 shows the drag polars or, in other words, the amount of drag for a given amount of lift (Anderson, 1999). It can be seen that the insertion of the fuselage "body" has almost no influence on C_d at $C_l = 0$ due to the inviscid calculation used in XFLR. Higher angles of attack correspond to higher lift coefficients at lower speeds. The drag due to the nonstreamlined fuselage, the rotor head, motor cooling, and all protrusions like antennae etc is added as an extra term. This is taken as a $C_{d_0} = 0.012$ based on the total wing area to lead to a more realistic drag. At low C_L or fast flight, this total drag is more than double the inviscid drag of the wing only. In all computations, the center of gravity is located at $x = 140.0$ mm from the central chord leading edge as shown in Figure A1.

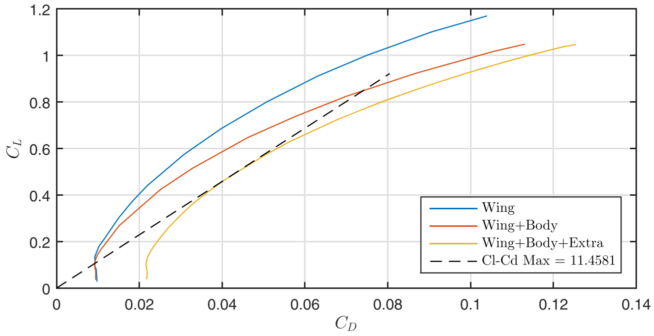

FIGURE 13 Lift-Drag computation using XFLR for a 4.5 kg *Delfta-Copter*. The figures show computed drag polars in the case of wings only, wings with ideal fuselage and the total vehicle including drag from rotor head and all protruding items like antennas. The best glide ratio $(C_L/C_D)_{max}$ is 11.4

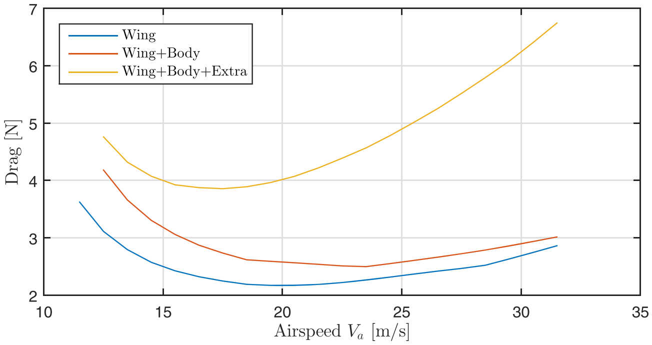

FIGURE 14 Total aerodynamic drag in function of airspeed V_a. When compared to the available thrust from the propulsion from Figure 7, one can see that at about 25 m/s the drag becomes larger than 5 N while the maximal achievable thrust with any blade setting becomes lower than 5 N. The theoretical maximal speed is thus found to be 25 m/s. If in reality the drag turn out to be higher, this would reduce the maximal speed

Using the drag polar from Figure 13 in the formula for lift $L = \rho/2V_a^2 \cdot S \cdot C_L$ with total wing surface $S = 0.496$ m^2 and ρ at sea level of 1.225 kg/m^2 the total drag can be computed. This is shown in Figure 14 and can directly be compared with the available propulsion thrust in Figure 7 to determine which flight speeds are possible, namely, according to these calculations, speeds of up to 25 m/s.

Figure 15 shows the power needed in function of forward speed given the previously computed drag polar (see Figure 13) and given a total system weight of 4.5 kg. When compared with the propulsion power required to hover with the same weight of 4.5 kg (see Figure 8), one can see that the wing requires an order of magnitude less power to stay in the air. From Figure 7, one can also see that, in pure helicopter mode without wing, the maximal airspeed where the rotor can still provide enough thrust to carry the entire weight of 4.5 kg or 44 N is about

---

[‡] MIKADO Model Helicopter.

[§] https://tracfoil.com/airfoils/uploads/files/profils/p/PW51i.dat.

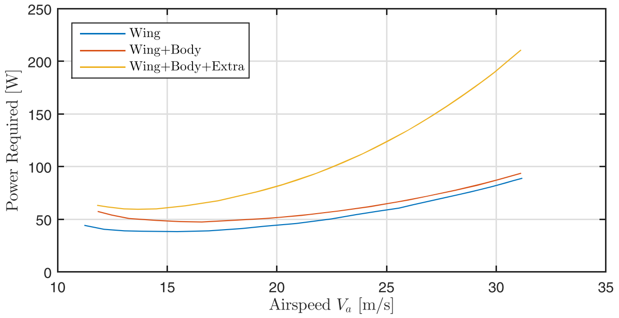

FIGURE 15 Required aerodynamic power in function of forward airspeed V_a computation using XFLR. It is clearly visible that especially at higher speeds, which correspond to lower C_L, a lot can still be gained by reducing the parasitic drag of the *DelftaCopter*. The actual power used depends on the propulsion setting used and all electrical losses

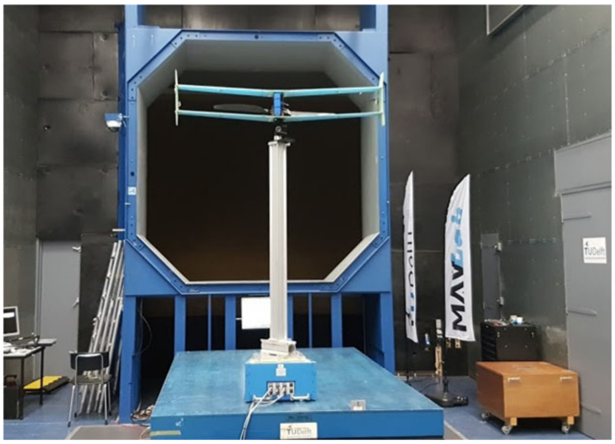

FIGURE 16 *DelftaCopter* in the Open Jet Wind tunnel of TUDelft. The tunnel outlet measures 2.85 m × 2.85 m and can reach 30 m/s wind speeds. *DelftaCopter* was mounted on a 1.8-m aluminum pole, which was standing on a force and moment balance. The *Y*-axis of the balance points into the tunnel opening. The *X*-axis points right in the picture and the *Z*-axis up

7 m/s. In that case, more than 500 W is used. In comparison, Figure 15 shows that thanks to its wings the *DelftaCopter* can fly using much less power and also reach much higher speeds.

5 | WIND TUNNEL ANALYSIS

In a typical scenario, the *DelftaCopter* would spend most of its time in forward flight. Therefore, optimizing the energy efficiency in forward flight is key to improving the range of the vehicle. While computations in Section 2 predicted an efficiency increase in forward flight with lower rpm, this could not easily be seen during flight tests. A possible explanation could be that the motor is less efficient at low rpm, canceling the performance gain from the propeller. To assess the propulsive efficiency and to find the optimal propulsion settings, a wind tunnel experiment was performed in the Open Jet Facility at Delft University of Technology. The vehicle was placed in the middle of the 2.85 m × 2.85 m wind tunnel outlet, with zero angle of attack. The *DelftaCopter* was rigidly attached to a pole, which was mounted on a force-moment balance below the wind tunnel outlet as shown in Figure 16.

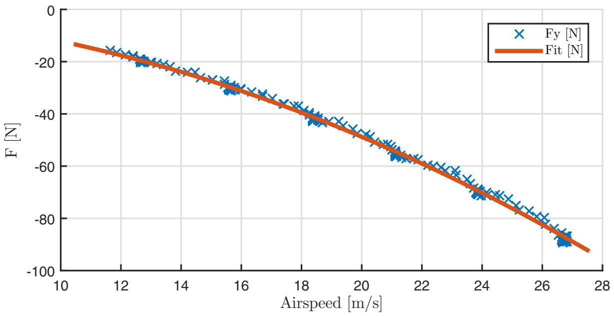

FIGURE 17 Drag of the pole in function of airspeed

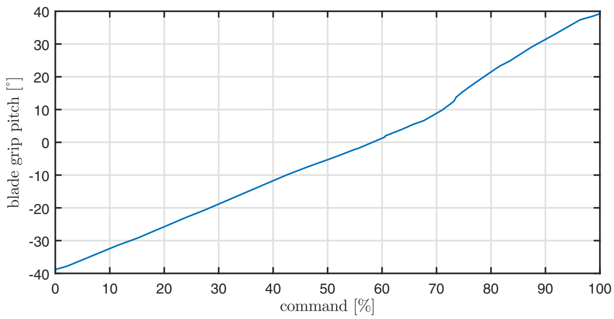

FIGURE 18 The nonlinearity of the collective pitch angle of the main rotor in function of the scaled servo command

First the drag of the pole and attachment without the *DelftaCopter* was measured. Figure 17 shows the resulting fit which finds a drag of $D = \frac{\rho}{2}V^2 \cdot 0.195$. Then the *DelftaCopter* is mounted on the pole in the middle of the open jet wind tunnel. Measurements are taken at several representative airspeeds, namely at 15, 19, 24, and 27 m/s. For each airspeed, the *DelftaCopter* parameters are measured through a range of main rotor collective pitch angles and power settings. The settings are selected manually such that no rpm, current, or motor temperature limitation is breached. The rotor is turning at all times as soon as the wind tunnel is blowing, and wind mills even when no power is applied.

One extra lab measurement is made to convert the servo pitch commands into an actual collective pitch angle. Using a *Heli-Max digital pitch gauge* applied externally to the rotor blade, 50 measurements were made manually from minimal pitch to maximal pitch. The nonlinearity of the rotor-head linkages is nontrivial as seen in Figure 18. A close-up photograph of the rotor head can be found in Section 8 (Figure 23).

During the wind tunnel runs as well as flights, all on-board data are logged onboard at 512 Hz using the onboard autopilot electronics and are visible in real time at 10 Hz through the autopilot telemetry. The logged data consisted of gyroscopic body rates and body accelerations, magnetometer readings, dual air pressure from inside the fuselage and from a static port in the wing, total pressure converted to airspeed, main rotor rpm, main battery voltage, auxiliary battery voltage, propulsion current, and main motor coil temperature. The electrical power plotted in this work concerns only the power used by the motors excluding the power of the autopilot and other electrical systems. Of special interest are the motor current and rpm together with the throttle and collective pitch settings. In parallel the wind tunnel system logged all forces and moments on the balance and the wind

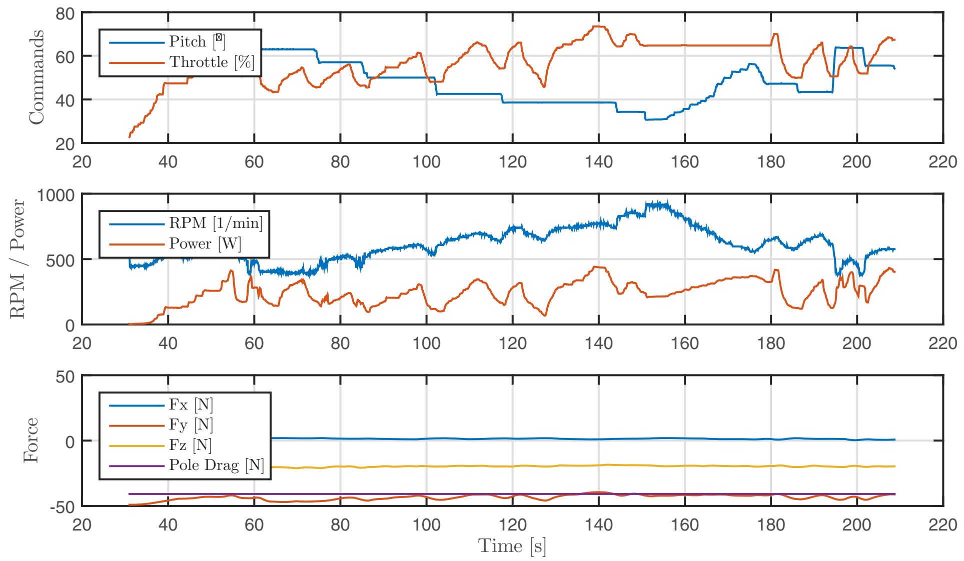

FIGURE 19 Raw wind tunnel data and on-board measurements for the tunnel setting at 19 m/s. For every pitch setting, all acceptable throttle settings are visited and the effect on power use and forward thrust is measured (see Figure 16 for the axis of the force balance)

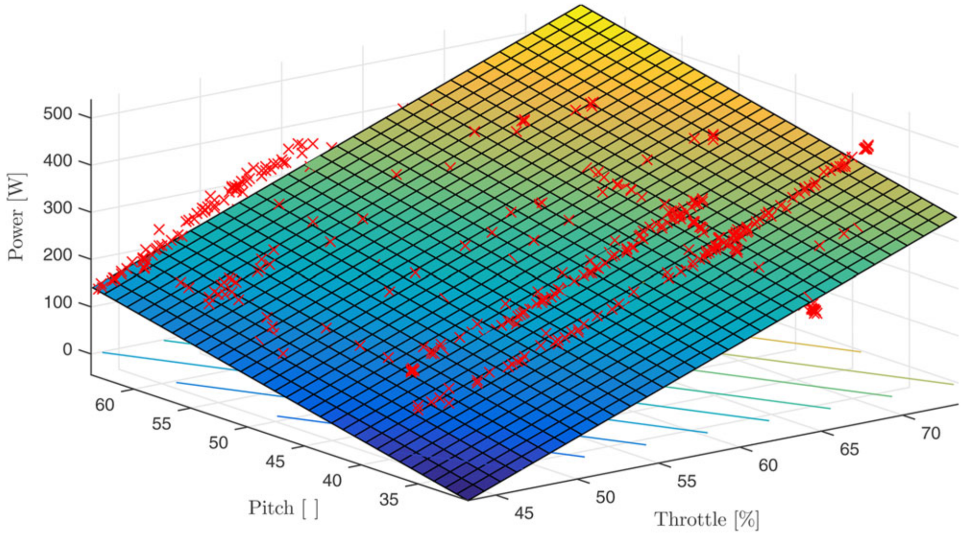

FIGURE 20 Measured power in function of pitch and throttle and planar fit showing rpm and pitch can be exchanged while keeping the same used power

tunnel calibrated airspeed (see Figure 19). From the data, it was expected to find a clear minimum power point, namely a throttle versus pitch setting where better efficiency could be obtained.

However, it was found that power and rpmwise, pitch and throttle can be exchanged without significant difference in power efficiency. Figure 20 shows a planar fit predicting the stationary used power based on the pitch and throttle input. This is not expected from the propulsion calculations. Section 2 predicted more efficiency at higher pitch and lower rpm at higher forward speeds like 19 m/s.

The main motor temperature was measured by the onboard avionics using an NTC[¶] thermistor glued to the inner coils of the main motor. Given the high motor temperatures observed at low rpm for a given power output, the motor efficiency is clearly shown to reduce with rpm. The reduced electric motor efficiency at lower rpm appears to precisely cancel out the gain in propeller efficiency at lower rpm. Identical results are obtained at other wind tunnel velocities. The plane fits the data very well with most off-plane points corresponding to temporary changes in power setting. Following the contour lines of the fit in Figure 20 from left to right, settings are found for pitch and throttle that consume the same amount of power but result in a different rpm.

Several other interesting observations can be made from the wind tunnel data. The force graph in Figure 19 for instance shows that the *DelftaCopter* does not have a lot of spare thrust in fast forward flight at 19 m/s. The thrust is observed through the balance force F_y. This force measures the negative pole drag, the negative *DelftaCopter* drag the positive *DelftaCopter* thrust. For steady cruise flight, F_y must be equal to only the pole drag. The F_y force only overcomes the pole drag at high throttle settings with at least 700 rpm. In other words, at too low rotor rpm the propulsion system seems unable to overcome the drag. This is in line with Figure 7, which predicted that at low rpm less thrust can be

---

[¶] Negative temperature coefficient.

created. The wind tunnel measurement shows that at a cruise speed of 19 m/s only an rpm of over 700 can still produce sufficient thrust, given the actual aerodynamics properties of the *DelftaCopter*.

Another very interesting part is seen from time 150–180 s where the throttle setting is kept constant and only the blade pitch is changed. The high pitch with constant throttle causes the rpm to reduce. The thrust minus drag, observed through the force F_y, first stays relatively constant and then starts to drop below 700 rpm. A constant throttle settings means a constant pulse width modulation (PWM) of the power on the motor and on a resistive load results in a constant power output. But the power in the *DelftaCopter* keeps steadily increasing with lower rpm from 900 to 600 rpm. This can only be explained by a lower inductance of the motor itself resulting in more current through the windings and more power loss in the motor; or in other words reduced motor efficiency.

Combining the theoretic predictions from Section 2 with the wind tunnel observations, several conclusions can be drawn.

First of all that the actual $(thrust - drag)$ is smaller than predicted since at speeds of 24 m/s no operating point can be found that overcomes drag. The predicted theoretical maximal velocity is shown not the be achievable during the wind tunnel test. Owing to the rough measurement of F_y however, actual flight tests are needed to find the exact maximal speed.

Also because the drag is higher than predicted, the rpm values below 700 cannot produce sufficient thrust to fly at 19 m/s cruise speed. Increasing the rpm allows to have more thrust.

The same is true for the optimal cruise speed. The optimal *forward speed over power* or *miles per mAh* cannot be extracted precisely from the wind tunnel data, but it could be seen through the heating motor and lack of thrust that speeds of 22–24 m/s become very inefficient. This means that the needed power to fly faster will be much more than shown in Figure 15, which does not take propulsion efficiency into account. Selecting higher flight speeds higher will significantly reduce the endurance of the *DelftaCopter*.

Overall it can be concluded that in the cruise regime, the *DelftaCopter* can operate at a large range of rpm and pitch settings without very significant change in efficiency, as the rotor efficiency increase at reduced rpm is canceled out by rotor efficiency loss.

To select an ideal rpm for the forward flight, the following observations were combined. The rotor needs time to spin up and can only hover at an rpm over 1,500. From Figure 9, we know an rpm below 1,000 is only useful for speeds over 22 m/s, but these speeds cannot be reached. The *DelftaCopter* can operate at a large range of rpm and pitch settings while cruising at about 19 m/s without very significant change in efficiency. Because it is safer in case of quick deceleration to hover, in its current form the *DelftaCopter* can best fly in forward flight with rotor speed above 1,000 rpm and use the blade pitch to select the desired speed in the control loops.

6 | ELECTRONIC DESIGN

To comply with the strict requirements of the Outback Medical Challenge (Clothier et al., 2015) and be allowed to fly beyond visual line of sight missions at up to 30 km distance, a custom electronic design was required. It consists of two independently powered circuits.

As seen in Figure 21, the first part is called flight termination device. This part has all the safety critical functions like driving actuators but also geo-fencing and long-range kill switches, motor unpowering, and arming.

All navigation and control functions together with the flight plan logic are in the second part called autopilot. Both parts are modifications of the Paparazzi-UAV (Brisset, Drouin, Gorraz, Huard, & Tyler, 2006) Lisa-MX autopilot (Gati, 2013).

Because of the number of extra functions and boards, like SD-card logging, master power cutoff, line drivers to modems in wings, power converters, current voltage, and temperature sensors, the design started to grow larger. To minimize interconnection failures and minimize the total weight, a custom printed circuit board (PCB) was designed with all needed functions, which is shown in Figure 22.

7 | ROTOR-HEAD DYNAMICS

Rotorcraft dynamics have been well studied for many years (Bramwell et al., 2001; Gavrilets, 2015; Johnson, 1980; Padfield, 2008; Prouty, 1995; Shim, Koo, Hoffmann, & Sastry, 1998; Stepniewski & Keys, 1979; Wagtendonk, 1996). But the properties of the light-efficient rotor on a large heavy fuselage found in the *DelftaCopter* are significantly different from what is seen in similar size conventional helicopters. In conventional helicopters, the gyroscopic effect of the rotor clearly dominates in the total system dynamics, and roll is steered by changing the lift at the front and back of the rotor. In conventional quadrotor control, the inertia of body clearly dominates over the precession of the propellers. Roll is steered by altering the lift of the left or right rotors. The *DelftaCopter* seems to be precisely in between both.

Early test-flight attempts showed very significant differences compared to conventional helicopter control, even in windless indoor hovering flight. Figure 24 shows how pitch commands were highly coupled with roll commands and vice versa. This coupling critically compromises the control of the platform in the real world. Before flight testing could be attempted, a solution to this attitude control problem has to be developed.

7.1 | Rotor

To investigate the dynamics of the *DelftaCopter* rotor and fuselage, a simplified model was derived (De Wagter & Smeur, 2016). Figure 25 illustrates the basic rotor model with rotor radius R and spinning rate ω. The flapping angle β is measured around the spring hinge K, and the feathering angle θ_B is periodic and follows the setting of the swash plate cyclic and collective control. The resulting equation of motion of a rotor blade can be written as

$$\ddot{\beta} + \frac{\gamma}{8}\omega\dot{\beta} + \left(\omega^2 + \frac{K}{I}\right)\beta = \frac{\gamma}{8}\omega^2(\theta_B) \tag{5}$$

in which β is the rotor angular rate, K is the spring stiffness, I is the blade flapping inertia, θ_B the blade pitch angle, and γ is the so-called *Lock*

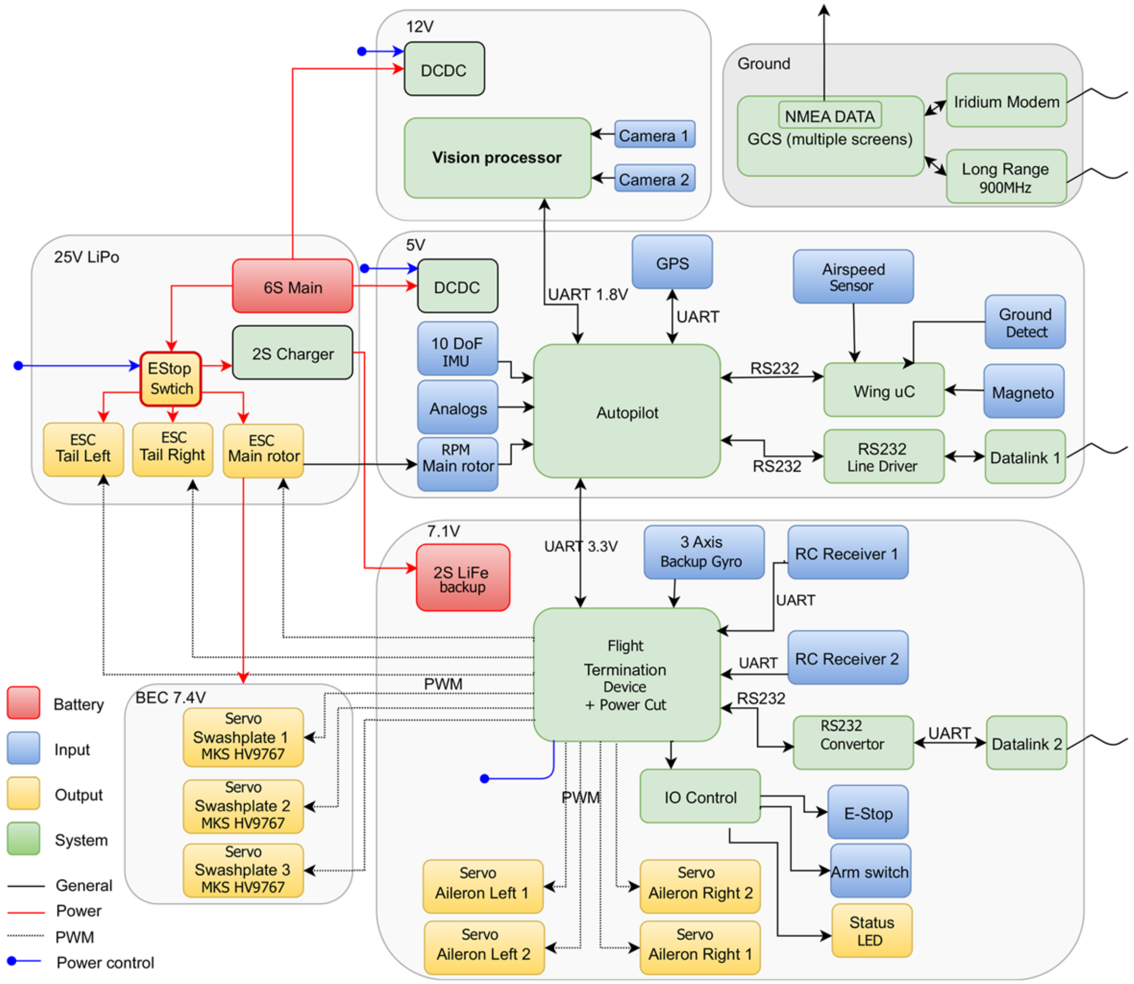

FIGURE 21 Schematic overview of the *DelftaCopter* electronics

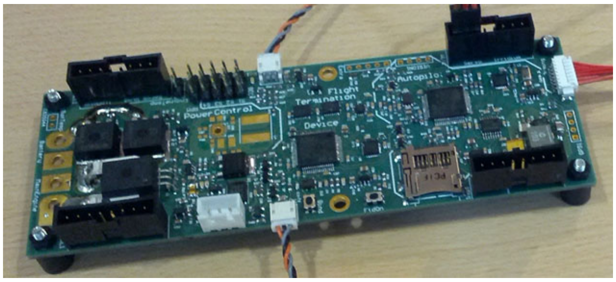

FIGURE 22 All central electrical functions of the *DelftaCopter* are integrated into a single board PCB for minimal weight and minimal interconnection failure. The four corner connectors lead to the systems in all four wings. From left to right, the board contains power, flight termination, and autopilot

number (Bramwell et al., 2001). The terms in Equation 5 from left to right relate first the inertia of the rotor, its aerodynamic damping, and the centrifugal and spring forces to the external excitation. This concise notation clearly shows that besides rotor rpm ω, the rotor dynamics depend mostly on a single entity *Lock number* γ:

$$\gamma = \frac{\rho c_{l_\alpha} c R^4}{I} \quad (6)$$

As given in Equation 6, the *Lock number* physically contains aerodynamic damping terms (air density ρ, chord c, rotor radius R, and lift coefficient c_{l_α}) divided by the blade flapping inertia I. In the *DelftaCopter* design, the *Lock number* is relatively high as the lift coefficient c_{l_α} and radius R are large whereas the mass and resulting inertia I are very small.

While Equation 5 shows the importance of rotor inertia in the response rate, it is not sufficient by itself to explain the couplings seen in Figure 24.

7.2 | Fuselage

To simulate and understand observed pitch and roll couplings, a fuselage model is added. Fuselage inertia is playing a crucial role in the control when the fuselage inertia becomes significant compared to the rotor inertia (De Wagter & Smeur, 2016). In the *DelftaCopter* the weight is spread over the very long wing with a lot of electronics like radios and antennas being placed in the wing tips for electronics reasons. The total weight of the *DelftaCopter* is over 4 kg whereas a rotor blade is only about 60 g and the rotor rpm is kept as low as practicable for power reasons. The fuselage inertia can be modeled as four point masses at locations l_x and l_y from the center as shown in Figure 26.

FIGURE 23 Close-up of the rotor head of the *DelftaCopter*. The swash plate has three gripping points at 120° from each other. The collective pitch can reach from −40° to 40°, which is double that of a conventional helicopter. The self-laminated blades with *MA409* section have high camber, a high lift coefficient, and 25 degrees of blade twist from root to tip. Hovering flight is performed at a designed tip angle of attack of around 10° with 1,500 rpm. In forward flight the tip angle of attack can change up to 50° at 500 rpm. The root angle of attack is then about 75°. The blade twist is made possible because the flow is always axial as the *DelftaCopter* transitions. This allows the rotor to be efficient from hover to fast forward flight

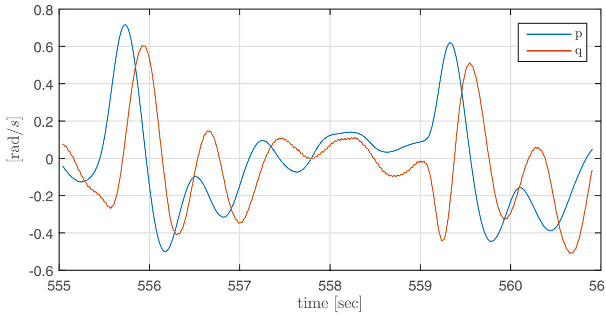

FIGURE 24 An early manual hovering test flight of the *DelftaCopter* with a manually tuned standard helicopter rate controller from the paparazzi-UAV autopilot (Brisset et al., 2006) showed that a doublet step input right ($t = 555$ s) and then left ($t = 559$ s) on roll rate p (rotation rate around body X axis) yields an undesired but very significant pitch rate q (rotation rate around body Y axis). Pilots described this undesired and delayed effect of pitch on roll commands as "*wobbling*"

The rotor and body interact with each other in the following ways. Even in case of a fully hinged rotor with $K = 0$, when the fuselage rotates, the rotor will automatically follow through the functioning of the swash plate. In case of nonzero K, an additional moment will be applied from the fuselage on the rotor whenever they are not in-line. The other way around a moment is transferred from rotor to fuselage through spring K, and another moment exists whenever the total lift is not going through the fuselage center of gravity. Forces through the swash-plate linkages are neglected.

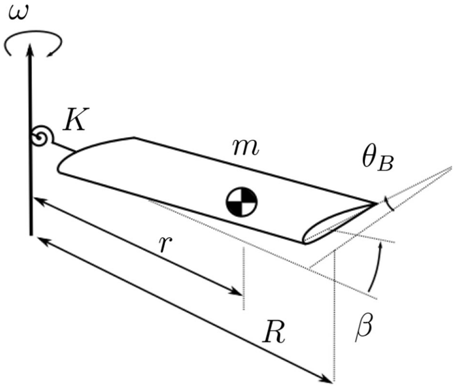

FIGURE 25 Simplified rigid rotor model of the *DelftaCopter* turning with angular rate ω, mass m, radius R, spring stiffness K yielding a flapping angle β and pitch angle θ_B

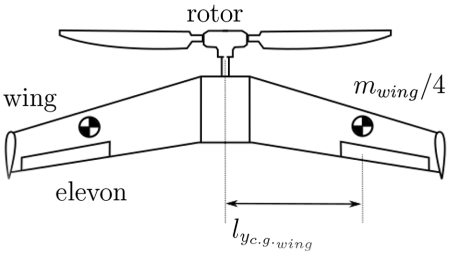

FIGURE 26 Body model

7.3 | Simulation

The combined effect of a light high-lift rotor and heavy nonsymmetric fuselage can be clearly visualized in simulation. A model with parameters found in De Wagter & Smeur (2016) is given a step input in pitch δ_x using a standard helicopter swash plate as modeled in Equation 7.

$$\theta_B = \delta_x \sin(\omega t) + \delta_y \cos(\omega t) \tag{7}$$

The resulting cross couplings between pitch and roll for different body inertia are shown in Figure 27. A pitch cyclic doublet δ_x is applied. The simulation results clearly show the resulting desired pitch rate q but show a highly different undesired coupling in roll rate p, which is totally different based on the inertia of the fuselage.

Please note that this simulation does not try to reconstruct the behavior depicted before in Figure 24. In the real flight, a rate control system was active which continuously adapted the control inputs, while the simulation in Figure 27 shows a constant cyclic deflection δ_x for a given amount of time. During the real flight, the rate controller or pilot applies a command in a certain direction, but the body reacts in a different direction. This causes the rate controller to adapt the command to compensate the new situation. In turn, the body dynamics react even further, and this continuous interaction results in the observed "wobbling."

In other words, when the rotational inertia of the fuselage is large in pitch and less in roll, then a pitch command on the rotor will start pitching up the rotor plane. The fuselage inertia counteracts this rotation and will result in a pitch down moment on the rotor. The precession of the rotor will turn this into a rolling motion.

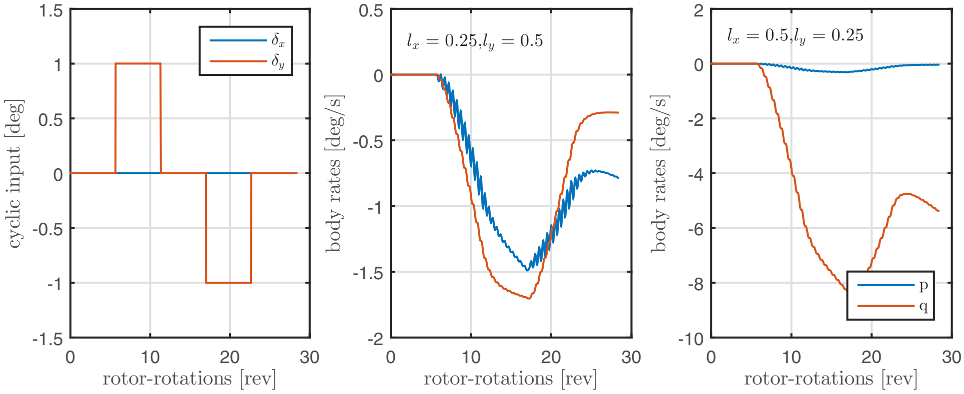

FIGURE 27 The influence of fuselage inertia on a free body. Differences in inertia distributions (see Figure 26 for the body model parameters l_x and l_y) are shown to influence the pitch response even in the simplified simulation. Although this simulation does not capture all aspects of the full rotor dynamics, it is nevertheless helpful understand the source of the coupling

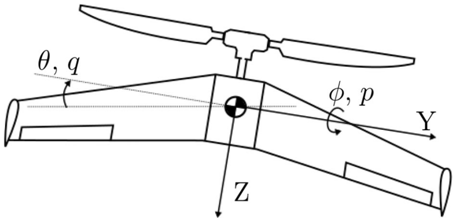

FIGURE 28 Body axis definitions, with the *X* axis defined by the right hand rule. The *X* axis points down in forward flight. *p* and *q* are the body rates around the *X* and *Y* axes, respectively

A controller for the *DelftaCopter* will therefore need to compensate for cross couplings in pitch and roll body motions.

8 | CONTROL

This section deals with the control laws used for the *DelftaCopter*. First consider Figure 28, which defines the body axis definitions. Angular rates around the *X*, *Y*, and *Z* axes are denoted with *p*, *q*, and *r* respectively. Together, they are denoted by the vector $\boldsymbol{\omega}$.

The *DelftaCopter* is able to autonomously fly a flight plan, with predetermined forward flight phases. To do this, the *DelftaCopter* is equipped with several actuators. On the main rotor, cyclic and collective pitch of the blades can be controlled. Collective pitch is changing the pitch of all blades collectively, whereas cyclic pitch can command a difference in angle of attack for two opposing blades. Tip propellers provide a moment around the body *Z* axis in hover, and four flaps, one on each wing, can provide a moment around the body *Y* and *Z* axes. The flaps are very effective in forward flight, but not during hover, when there is a lack of airflow. This is why the tip propellers are crucial during hover, but are turned off in forward flight.

The control of the *DelftaCopter* can be divided into an inner and an outer loop: The inner loop controls the angular rates and the attitude, whereas the outer loop controls the velocity and position, making use of the inner loop.

8.1 | Attitude control

The inner loop control of the *DelftaCopter* is essentially a proportional integral and derivative (PID) controller, but it is split into a common attitude part and a different rate part for the flaps and the rotor. The control of the attitude is done in quaternions, because tail-sitter hybrid UAV pitch down 90° or more to transition from hover to forward flight and at these angles Euler representations reach singularity (Fresk & Nikolakopoulos, 2013). A reference for the angular rates is constructed from the vector part of the error quaternion times a gain K_q:

$$\boldsymbol{\omega}_{\text{ref}} = K_P \begin{bmatrix} q_x & q_y & q_z \end{bmatrix}^T_{\text{err}} + K_I \sum_i \begin{bmatrix} q_x & q_y & q_z \end{bmatrix}^T_{\text{err}} \tag{8}$$

where the error quaternion is calculated using the Hamilton product according to

$$q_{\text{err}} = q_{\text{ref}} \otimes q_m^* \tag{9}$$

Here * denotes conjugation (Fresk & Nikolakopoulos, 2013). Equation 8 contains the integrator term, which sums the quaternion error over every discrete time instant *i*. The gain K_I can be tuned to remove steady-state errors.

This covers the proportional and integral terms. From the reference angular rate, the angular rate error is calculated as

$$\begin{bmatrix} p_{\text{err}} \\ q_{\text{err}} \\ r_{\text{err}} \end{bmatrix} = \boldsymbol{\omega}_{\text{err}} = \boldsymbol{\omega}_{\text{ref}} - \boldsymbol{\omega} \tag{10}$$

Then, the commands are calculated by multiplying the angular rate error with the linear rate gain K_D. Different PID gains are implemented for hover and forward flight.

The commands then pass through the control allocation, which sends the commands to the various actuators for the flaps, the tip motors, and the swash plate. The flaps and swash plate are both always active at the same time in hover and in forward flight and are given 100% authority. The tip motors are only active in hover. For the flaps and tip motors, commands are linearly mixed passed on to the actuators as it is clear which flap controls which axis.

$$\begin{bmatrix} \delta_{\text{elevator}} \\ \delta_{\text{ailerons}} \\ \delta_{\text{tipprops}} \end{bmatrix} = \begin{bmatrix} K_q \cdot q_{\text{err}} \\ K_r \cdot r_{\text{err}} \\ K_r \cdot r_{\text{err}} \end{bmatrix} \tag{11}$$

But, as the theory presented in the preceding heading shows, the main rotor is a bit more involved, because it is not known which swash-plate deflection δ_x and δ_y results in which moments and this also depends on body rates. This is explained in Subsection 8.1.2.

8.1.1 | Swash-plate actuator mixing

Once the desired cyclic commands δ_x and δ_y are computed, which rotate the swash plate around the body X and Y axes, respectively, the final step is to compute the needed actuator deflections to move the swash plate as desired. Three servos δ_{s1}, δ_{s2}, and δ_{s3} are used to control the plate shown in Figure 23 using Equations 12–14.

$$\delta_{s1} = \frac{\sqrt{2}}{2}\delta_x + \frac{\delta_y}{2} \tag{12}$$

$$\delta_{s2} = -\frac{\sqrt{2}}{2}\delta_x + \frac{\delta_y}{2} \tag{13}$$

$$\delta_{s3} = -\delta_y \tag{14}$$

8.1.2 | Compensating the *DelftaCopter* rotor dynamics

Using the on-board SD logging, data were collected in flight to identify the coupled vehicle dynamics. From Section 7, the angular acceleration in pitch $\dot q$ and roll $\dot p$ are expected to result from the cyclic inputs δ_x and δ_y, the rates in roll p and pitch q. To fit their relative influence, coefficients were introduced to fit the influence of the former variables on the pitch and roll accelerations: C_{A_B} which reflects the influence of input A on output B for inputs p, q, δ_x and δ_y on outputs $\dot p$ and $\dot q$. Offsets $C_{O_{\dot p}}$ and $C_{O_{\dot q}}$ are added to the fit to compensate for trim errors. The fits are referred to as $f_p()$ and $f_q()$. The control model is shown in Equations 15 and 16:

$$\dot p \approx f_p() = C_{O_{\dot p}} + C_{\delta_{x\dot p}}\delta_x + C_{\delta_{y_{\dot p}}}\delta_y + C_{p_{\dot p}}p + C_{q_{\dot p}}q \tag{15}$$

$$\dot q \approx f_q() = C_{O_{\dot q}} + C_{\delta_{x\dot q}}\delta_x + C_{\delta_{y_{\dot q}}}\delta_y + C_{p_{\dot q}}p + C_{q_{\dot q}}q \tag{16}$$

Figure 29 shows the angular acceleration in roll and pitch along with the best fit of the coefficients for a short indoor flight fragment where the *DelftaCopter* keeps a constant rpm of 1650 rpm during a step in roll of approximately 20°. All signals were filtered with a second-order filter with a cutoff frequency of 15 rad/s. From the figure, it can be seen that this model fit can explain most of the behavior for this part of the flight. The coefficients that were found using the data shown in Figure 29 are given in Table 2.

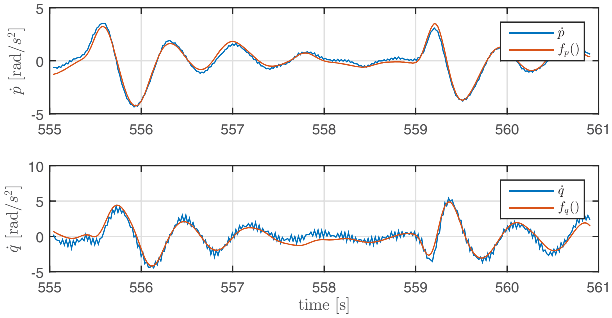

FIGURE 29 Fitting the control inputs and body rates to body accelerations $\dot p, \dot q$. The best model fits $f_p(), f_q()$ relate well to the observed filtered angular accelerations

TABLE 2 Identified parameters

Coefficient	$\dot p$	$\dot q$
C_O	−2.4661	−2.8847
C_{δ_x}	0.0032	−0.0044
C_{δ_y}	0.0011	0.0073
C_p	−0.5703	7.4479
C_q	−3.4308	−3.4487

When looking closely at the coefficients for C_p and C_q in Table 2, they confirm that a roll rate causes a pitch acceleration and vice versa.

Taking into account the identified couplings, the linear controller is revised to

$$\begin{bmatrix} \delta_x \\ \delta_y \end{bmatrix} = G^{-1}\begin{bmatrix} K_p \cdot p_{\text{err}} + q \cdot C_{q_{\dot p}} \cdot K_c \\ K_q \cdot q_{\text{err}} + p \cdot C_{p_{\dot q}} \cdot K_c \end{bmatrix} \tag{17}$$

where p_{err} and q_{err} are the difference between the desired rates and the actual rates of the vehicle, and G is given by Equation 18. K_p and K_q are gains that can be tuned.

$$G = \begin{bmatrix} C_{\delta_{x_{\dot p}}} & C_{\delta_{y_{\dot p}}} \\ C_{\delta_{x_{\dot q}}} & C_{\delta_{y_{\dot q}}} \end{bmatrix} \tag{18}$$

An in-flight tuning parameter K_c is introduced with a value between 0 and 1. It was introduced to gradually enable the compensation of angular acceleration due to rates. Test flights showed that a value of $K_c = 0.5$ gives better results than a value of $K_c = 1$. This may be caused by actuator dynamics, as a control moment cannot be instantly generated when a rate is measured. More research is necessary to better explain why $K_c = 1$ still gives a wobble.

Figure 30 shows the measured angular rates of the vehicle during some pitch maneuvers in the first part of the flight and some roll maneuvers in the second part of the flight. The rates were filtered with a second-order filter with a cutoff frequency of 25 rad/s. In the bottom figure, the roll angle ϕ and pitch angle θ, as defined by ZYX Euler angles, are shown. From Figure 30, it can be seen that no wobble is present, and the motion in roll and pitch is uncoupled. When compared back to the initial situation in Figure 24, it can be seen that the control was highly improved.

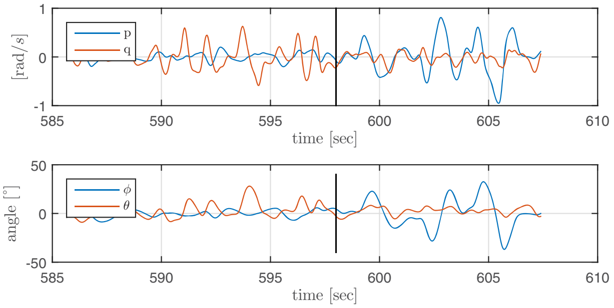

FIGURE 30 Manual test flight in attitude mode to confirm the observed coupling as seen in Figure 24 has been resolved. In this flight, a K_c of 0.5 was selected to yield the best results. Before time $t = 598$ the test pilot was applying mainly pitch commands, and after mainly roll commands while keeping the vehicle in the flight area

For every change in fuselage inertial or rotor inertia or rotor rpm, new values need to be computed. In particular, during forward flight, if the rotor rpm is decreased, other parameters will be needed. Since wind tunnel testing in Section 5 showed the little decrease in efficiency at higher rpm, it was chosen to fly forward with the same rpm as in hover so a single set of coefficients needed to be computed.

8.2 | Horizontal position control

The horizontal position control differs based on the flight mode: hover or forward flight.

8.2.1 | Hover

The control of the horizontal position during the hover phase is done with an incremental nonlinear dynamic inversion (INDI) controller. A detailed description of this control method, along with experiments that show the performance, is provided in previous work (Smeur, de Croon, & Chu, 2016). The rationale behind this controller is that the accelerometer measurement provides the sum of forces acting on the vehicle. The gravitational force vector is not measured by the accelerometer and has to be added using the estimate of the attitude. This sum of forces contains external forces acting on the airframe, but also the control forces, such as the thrust vector. Therefore, a change, or *increment*, in acceleration can be achieved by incrementing the control forces. Because disturbances are directly measured by the accelerometer, influences from gusts can be largely mitigated.

The position control in hover is purely based on the thrust vector and does not take the wing into account. However, because of the large wing area, wind gusts can result in significant forces. For a controller that does not take the accelerations into account, this can lead to considerable tracking errors. However, because these forces are directly picked up by the accelerometer, with INDI they are immediately compensated, even though no knowledge of the wing is provided.

8.2.2 | Forward flight

During forward flight, the goal of the horizontal navigation is to fly toward waypoints, and the direction of flight is controlled by making coordinated turns. Vehicle pitch and roll are controlled with a PID controllers based on altitude error and heading error. For the heading, a coordinated turn is made purely on a feedforward basis, where the heading change is proportional to the tangent of the roll angle:

$$\dot{\psi} = \frac{g \cdot \tan(\phi)}{V_A} \tag{19}$$

Because there is no measurement of the sideslip, in the controller it is assumed that the sideslip is zero, and the lateral stability of the *DelftaCopter* actually reduces it to zero.

8.3 | Altitude control

During hover, the vertical axis is controlled by a PID controller, which only uses the thrust as an input. During forward flight, the vertical axis is controlled with the pitch angle, through a simple proportional gain. If the aircraft is pitching up from its nominal cruise pitch angle, thrust is added proportionally to the additional pitch angle to maintain airspeed. Additionally, if the aircraft is rolling, there is a proportional feedforward control action that pitches up, since more lift will be needed during turns.

8.4 | Transition

To keep things simple, the *DelftaCopter* was either in hover mode, or in forward mode. Transitions between the two flight modes were planned ahead and governed by the flight plan. Practically, during a transition the roll angle is kept zero and the heading is kept constant, whereas the pitch angle is gradually increased or decreased over the course of 3.125 s. When going from hover to forward flight, the tip propellers are turned off when the transition is halfway. At that point, the flaps have become effective enough to counter the rotor torque due to the increased airflow, and energy is saved by not using the tip propellers.

The downside of having predetermined transitions is that the vehicle will not be able to cope with strong wind. The hover mode is capable of, taking into account quite conservative maximum bank angles, flying at roughly 7 m/s. That means that this will be insufficient to hold a position in winds stronger than this.

Preferably, the controller would be capable of controlling any airspeed from zero up to cruise, whereas the transition is managed by the position controller itself. This would allow flight at any wind speed below the maximum flight speed.

Another downside of this transition method is that it is not able to keep the altitude constant, as feedback during the transition is limited. In practice, large altitude deviations occur when transitioning back to hover, when the increase in pitch often leads to an altitude increase of 10–20 m. This will be improved in future work. However, even though the transition is not very precise, it is very reliable. In all test flights we performed, it did not lead to a crash once.

9 | VISION

The *DelftaCopter* was equipped with a state of the art computer vision system as can be seen in Figure 31: a prototype of the Parrot S.L.A.M.dunk.

FIGURE 31 The S.L.A.M.dunk vision system

TABLE 3 S.L.A.M.dunk prototype properties

Processor	Nvidia Tegra TK1
Cameras	1280 × 1024 RGB
Depth map	640 × 480
Frame rate	30 fps
Stereo base line	20 cm
Lenses	Fish eye
Sensors	10-DOF IMU and sonar

Our prototype[#] S.L.A.M.dunk API delivered a 96 × 96 pixels depth map which, if overlaid over the original camera image, was the center 640 × 480 pixel range cropped from the full 1280 × 1024 camera resolution. The depth map was generated at 30 fps, by means of semiglobal matching accelerated by the GPU. On the *DelftaCopter*, the S.L.A.M.dunk looked straight down toward the ground when in hover mode, as can be seen in Figure 35.

This system was used for (1) detection of Joe, (2) landing spot selection, (3) obstacle avoidance during landing, and (4) determining the moment of touchdown. Lastly, a feature was devised to automatically calibrate the attitude error between the airframe and the S.L.A.M.dunk. The hardware specifications are shown in Table 3.

9.1 | Finding Joe

The competition organizers only provide an approximate GPS position of bush walker Joe (±100 m accuracy) (UAVChallenge, 2016) while strict requirements were imposed on landing locations. Therefore, the vision system needed to search and pinpoint the exact position of Joe. The Medical Outback challenge rules dictate to keep a minimum distance of 30 m from Joe in all directions, to comply with CASA (airspace regulatory body in Australia) regulations. In practice, this meant the *DelftaCopter* needed to maintain a minimum height of 40 m while searching, to account for height measurement errors and gusts. Joe was to be visible in a field near a farm, wearing normal blue jeans and an Australian Akubra head.

Owing to limitations imposed by the fish-eye lens, the overall quality of the images of Joe taken from a moving and vibrating platform at 40 m height was low. Joe was reported to be standing upright, which makes a birds-eye view advantageous to detect pose and human parts features (Rudol & Doherty, 2008). However, this nonperpendicular view results in an increased observation distance to Joe, and therefore even smaller pixel representations. No example data of the Australian scene or Joe was available beforehand, complicating methods that need many training examples (De Oliveira & Wehrmeister, 2016), and due to ongoing development on the *DelftaCopter* itself vision test flights on the final platform were scarce. Therefore, emphasis was placed on an algorithm simple enough to test and tune at the last moment on the Australian scene.

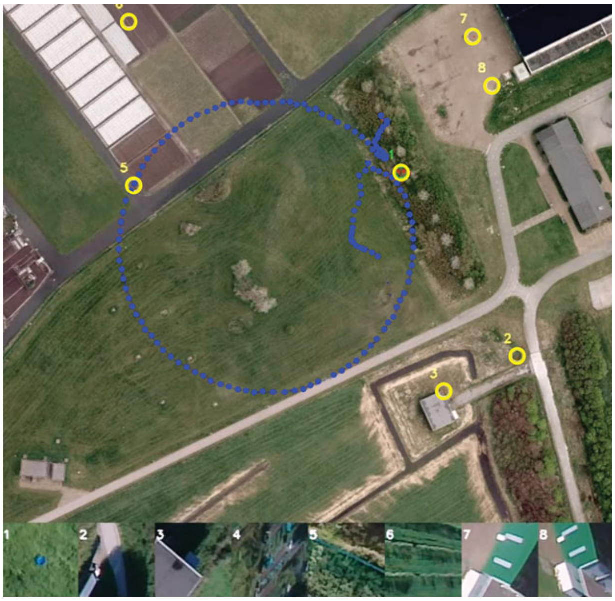

FIGURE 32 Person detection system

Instead of using a real human for Joe, the competition organization used a full-size dressed dummy. This means no movement or thermal features could be used (Gaszczak, Breckon, & Han, 2011). Instead, a simple color filter (i.e., an hue saturation and value (HSV) range) plus a shape filter (i.e., an OpenCV simple blob detector) was used as a salience detector to detect possible Joes. These were clustered based on their projected GPS locations through time. The projected GPS position of a possible Joe is determined by projecting its image coordinates to the ground based on the camera angle to the ground (including the attitude of the aircraft). This results in a distance and heading from the current position of the aircraft, which is added to the measured GPS position of the aircraft. If a possible Joe is detected closer than a distance threshold to where a previous Joe was detected, they are merged into a cluster of which the cluster center position is the weighted average of all Joe positions in the cluster. The best exemplary thumbnail of each cluster is selected, cut out, and updated as a better view angle became available. These thumbnails, accompanied with their projected GPS positions and Joe likelihood scores (cluster sizes) were calculated, and sent over the data link to the ground control station. Priority is given to the biggest cluster (i.e., the most possible Joe sightings through time). A video of the Joe detection algorithm in action can be viewed online[‖].

At ground station control, the vision operator was shown an interface with a map, geolocated numbers, and a list with accompanying thumbnails as shown in Figure 32. The blue dots show the flight path,

---

[#] The unit used in the *DelftaCopter* was a prototype product in development, the S.L.A.M.dunk will have improved specifications at release time.

[‖] Joet detection: https://www.youtube.com/watch?v=GVTHuwg3VJY.

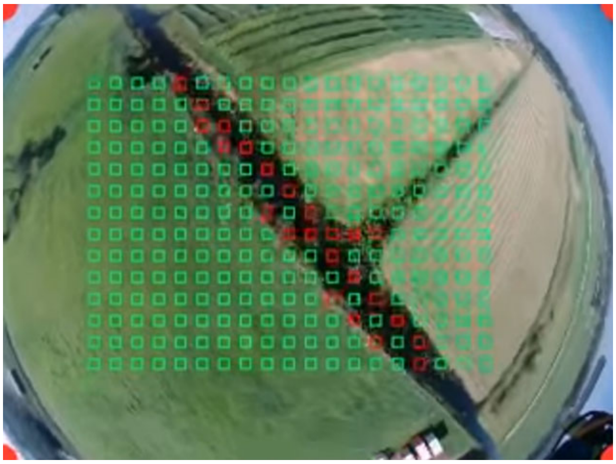

FIGURE 33 Landing site classification into land-able and dangerous based on texture comparison

the red dots show Joe sightings, the yellow circles show the average location of the clustered red dots, and the green circle shows the winning Joe sighting based on the highest Joe likeliness score (i.e., the biggest cluster). During the competition flight, a flight pattern in the shape of a *W* was preprogrammed to cover the whole possible area.

9.2 | Selecting a landing spot

During the search for Joe, the surface was analyzed at the same time for landibility. Reference textures of areas with a known good surface (farmers land, grass, desert, road, etc.) and bad surface (water, trees, roofs, etc.) were annotated beforehand, and during flight classified with a simple Euclidean distance texture comparison (Cover & Hart, 1967). The texture 11 × 11 pixel texture patches were subsampled from the video stream as shown in Figure 33. The advantage of using a simple classifier was that it was very quick to adapt it to new field conditions encountered in a different area and did not require large training data sets and would even allow inf-light updates to the classifier by adding new positive or negative samples to the reference sets. A video of the on-board results can be viewed online.[**] On this result, a blobfinder was applied and the biggest blob close to the selected Joe was automatically converted to the landing waypoint.

9.3 | Obstacle avoidance

The landing site is in a natural, unstructured and unfamiliar environment, which means the likelihood of unforeseen obstacles such as houses or trees is high. Some assumptions on the environment are made. It is assumed that in the targeted area the surface is commonly flat enough for the *DelftaCopter* to land. Furthermore, although obstacles are assumed to be of frequent occurrence, they are assumed to be sparsely located such that enough room exists between (small groups of) obstacles to land.

During hover, the S.L.A.M.dunk is looking downwards and an algorithm based on the depth map provided by the S.L.A.M.dunk is implemented to land safely. The depth map can detect obstacles up to approximately 30 m away but has significant noise in the farthest 10 m. To prevent false positives from the depth map, the landing is only enabled at heights lower than 20 m above ground level. The inertial measurement unit (IMU) information is used to determine the pixel location in the image that is straight down. This is especially important in the *DelftaCopter* design that can fly at considerable bank angles in hover in windy conditions. During landing, a circular area in the image around the current straight down pixel is selected. A moving average depth is calculated in this area ito determine the closest distance, the average distance, and the minimum distance. Flatness is defined as the closeness between the minimum and maximum to the average. When the flatness is sufficiently high according to a threshold, the surface is considered safe for further fast descend. Otherwise, the aircraft is repositioned toward the area with the greatest depth.

A proportional gain is steering the *DelftaCopter* laterally away from the global minimum of the moving average depth around the aircraft while the descend speed is decreased. Several tests showed the *DelftaCopter* to be able to avoid all obstacles visible in a stereo vision depth map during landing, like, for instance, trees and structures. A video of the on-board results can be viewed online.[††]

9.4 | Touchdown

To make repeatable precise and smooth landings, predicting the exact moment of touchdown is very important. The S.L.A.M.dunk can measure the height to the ground from over 20 m down to 10 cm by mixing the sonar and the stereo depth. This precise height combined with the *DelftaCopter* attitude information from the autopilot provides the required information to time landings successfully repeatedly. A video of a full autonomous landing can be viewed online.[‡‡]

9.5 | Attitude error calibration

The S.L.A.M.dunk was designed to be removable to allow easy access to the battery and electronics inside the *DelftaCopter*. This can cause a possible discrepancy in the attitude between the camera and the airframe, depending on the mounting process. However, an exact attitude measurement is necessary to precisely geolocate obstacles and Joe. Using the difference between the IMU embedded in the S.L.A.M.dunk and the IMU of the autopilot, the offset in attitude is determined automatically during the start-up phase. This lowers the requirements on the mounting system significantly.

10 | FLIGHT PERFORMANCE

The design work from the previous sections eventually resulted in a stable unmanned aircraft that could perform transitions between hover and forward flight. In this section, the flight performance of the *DelftaCopter* is evaluated.

[**] Landing spot classification: https://www.youtube.com/watch?v=RQ6F2ccMv8g.

[††] Landing obstacle avoidance: https://www.youtube.com/watch?v=2eCi8VJiDcs.

[‡‡] Full autonomous flight: https://www.youtube.com/watch?v=Bm8BBPKH7w4

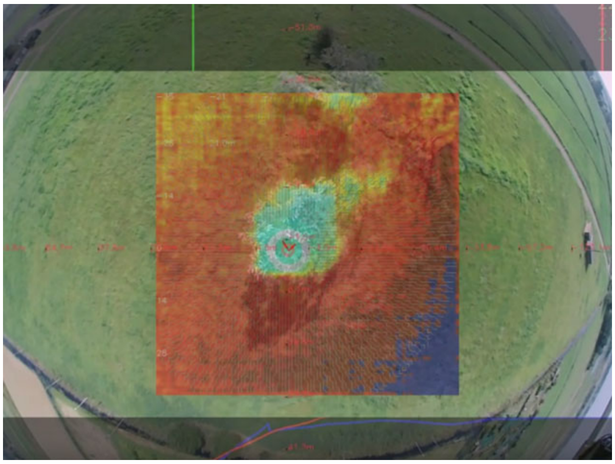

FIGURE 34 The landing avoidance system based on the S.L.A.M.dunk disparity map. The colored disparity map in the center of the image clearly shows a high tree

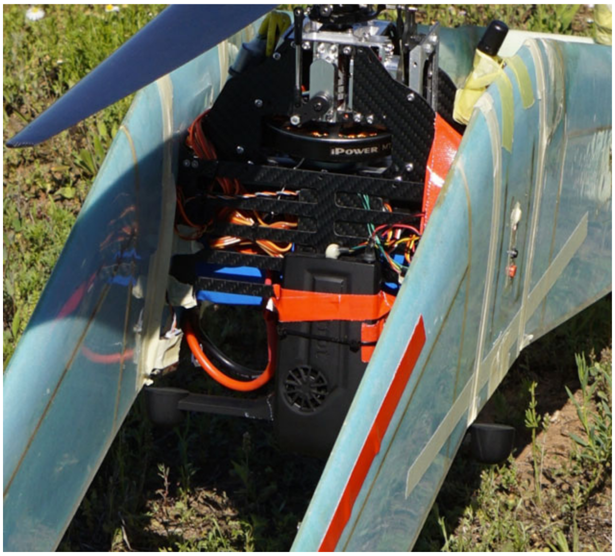

FIGURE 35 The S.L.A.M.dunk vision system was mounted on the *DelftaCopter* looking away from the main rotor. In hovering flight, this means the camera has a perfect view of the ground, and in forward flight the camera looks backwards. Thanks to the wide field of view fish-eye lenses, the camera can nevertheless still look vertically down during forward flight

10.1 | Transitioning flight

Figure 36 shows a flight with six transitions from hover to forward flight and back. During a transition from hover to forward, the *Delfta-Copter* has a small increase in altitude due to the applied power. During the transition from fast forward flight back to hover, a much more significant altitude overshoot is observed of about 17 m due to excess energy during the fast transition. The flight in this figure is performed in a very confined area of about 150 m × 150 m, and in forward flight the *DelftaCopter* is turning most of the time. Figure 36 also shows how during every hover the engine temperature is rising due to the increased load.

Figure 37 shows a close-up of a transition from the same flight as Figure 36. The figure shows a smooth transition form hover at body pitch angles around zero, and a linear transition to body pitch down toward $-90°$ with the X axis pointing to earth in that configuration. During the short 30 s forward flight, four turns are performed during which the pitch angle is increased (less negative) to maintain the correct altitude. The altitude has large peaks during the transition. During the transition from hover to forward flight, throttle is increased significantly to accelerate. The result is a peak in power used. During the forward flight, altitude is well maintained even during the turns. During the transition from forward flight to hover, the vehicle has a lot of excess energy to dissipate. The transition is made based on timing, and the excess energy results in a climb of more than 15 m. The hover controller then returns the vehicle to the desired altitude.

10.2 | Efficiency testing

During another test flight shown in Figure 38, an attempt is made to find the optimal forward flight regime. According to the design from Section 2, a lower rotor rpm in forward flight should be more efficient. The actual flight data does however not clearly show an efficiency increase. This corresponds exactly to the wind tunnel observations from Section 5. The rising motor temperature shows that the high motor load does decrease the electrical efficiency. Since no loss of total efficiency is observed, this means the propeller efficiency indeed increases but is undone by the loss of electric motor efficiency.

10.3 | Competition flight

The goal of the *DelftaCopter* was to bring medical aid to an isolated person in need. This was tested during the 2016 Medical Express competition held in Dalby, Australia. The remote location of "Joe," namely the person in need, was never visited before a,nd his appearance was not known. On average, weather conditions were good with only mild ≈ 5 m/s winds, no precipitation and more than 10 km visibility. However, there were occasional whirlwinds, sucking sand and butterflies 100 m into the air. The team had 15 min to set up all equipment like laptops, antennas, and prepare the *DelftaCopter*. After a thorough preflight inspection, the *DelftaCopter* performed a perfect autonomous takeoff and transition to forward flight in front of all spectators.

As can be seen in Figure 39, the flight started at Waypoint 1 and the path passed the takeoff location again at Waypoint 5 after approximately 10 km of flying. This was done for safety reasons. Waypoint 3 was located over agricultural areas with very little danger for people on the ground. Safely flying this return segment increased the chances that the UAV was operating properly before attempting the flight over roads near Waypoint 6 and toward a farm at Waypoint 9. The total traveled distance to Joe is 21.1 km or 11.4 Nm one-way. During the flight all va,riables had to be given in aviation units, namely *Kt*[§§] for airspeed, *ft*[¶¶] for altitude, and *Nm*[##] for distance.

During the flight, all systems worked as desired and performance was consistent with all the test-flying data. The *DelftaCopter* was

---

[§§] 1 kt (knot) = 0.51388 m/s

[¶¶] 1 ft (feet) = 0.3 m

[##] 1 Nm (nautical mile) = 1,852 m

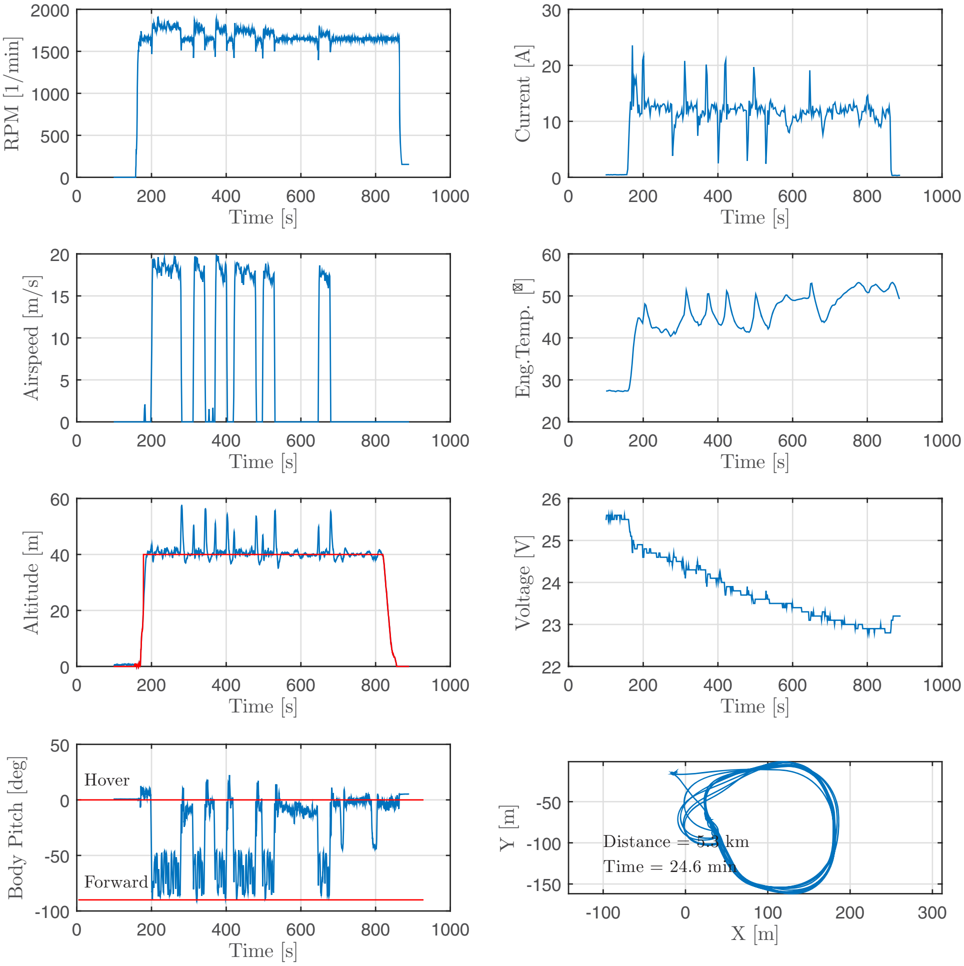

FIGURE 36 Test flight containing six transitions from hover to forward flight and back

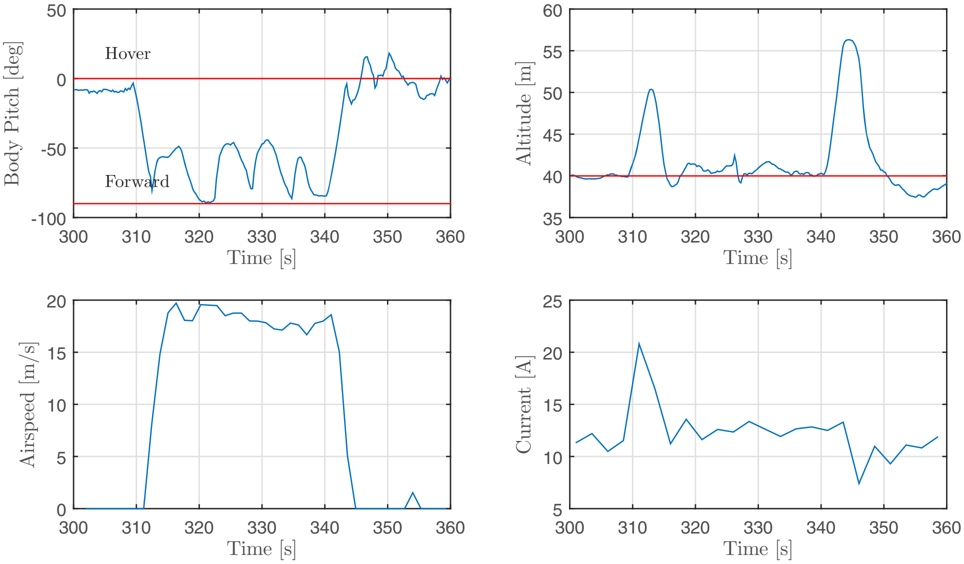

FIGURE 37 Close-up of a single transition. The *DelftaCopter* is starting from hover and transitions to forward flight. The current used increases to over 20 A during the acceleration phase and altitude increases during the open-loop transition. It then flies a square pattern while the body pitch angle is used to control altitude. During each of the four turns, significant pitch up is required during the turns to keep the altitude constant. Finally, the *DelftaCopter* transitions back to hover in a 3 s open-loop maneuver where all excess kinetic energy is transformed into altitude

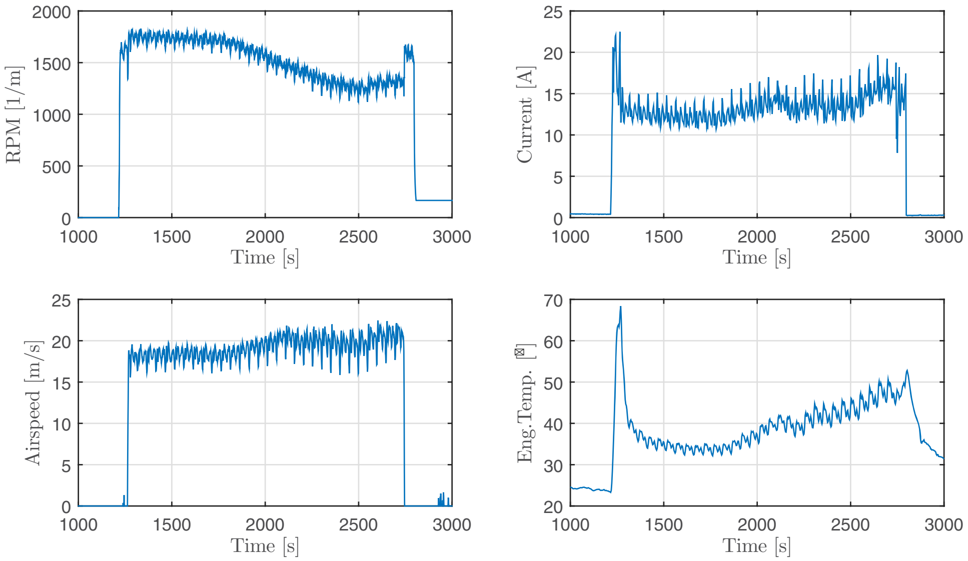

FIGURE 38 In search for the optimal rotor rpm for most efficient forward flight, a long outdoor flight on a very calm evening was performed in which a large range of pitch and throttle settings were tested

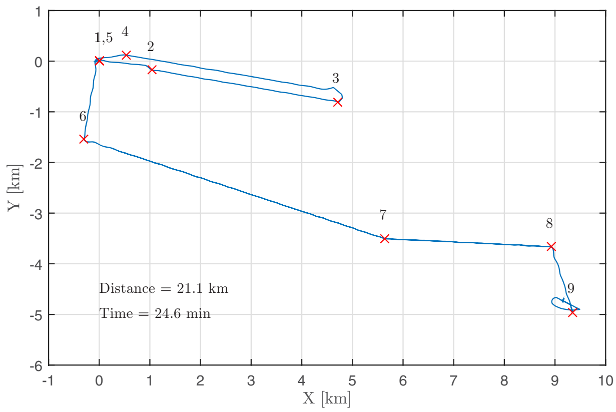

FIGURE 39 Competition flight ground track. The flight starts at Waypoint 1 and searches for Joe around Waypoint 9. Including the hovering takeoff and landing, the flight to Joe took 24.6 min and the total distance of the flight was 11.4 Nm or 21.1 km

carrying a full 10.5 Ah six cell lithium-polymer battery weighing 1.6 kg and the Parrot S.L.A.M.dunk stereo camera. Total weight was 4.3 kg.

Figure 40 shows that its cruise airspeed was a little under the designed 40 kt, which corresponds to 20.5 m/s. The eastern wind meant that *DelftaCopter* has a head-wind during most of the flight; therefore, the altitude was selected as low as allowed to exploit wind gradient effects, which yields lower wind speeds close to the ground. The return flight was expected to be shorter as the wind would then become a tailwind.

Unfortunately, the mission was not completed since no return flight was performed as can be seen in Figure 40. Instead *DelftaCopter* made a controlled landing into a tall gum tree.

As is often the case in aviation, many factors contributed to this mishap. For starters, the default coordinates of the visual landing waypoint were not defined, meaning it would default at the takeoff location. Second, while computer vision parameters were shown to work fine in test setups, at the actual competition they turned out to be too restrictive, meaning at first no detection was made. To make matters worse, due to a laptop USB problem during the very short setup time, the communication links via the 900-MHz and Iridium links were arriving on two different laptops. This resulted in lower situational awareness as not all parameters arrived on both, also causing extra communication overhead between operators. One of the biggest contributing factors which escalated previous problems was that very fast decision making was required when arriving at the location of "Joe," as the operation of the *DelftaCopter* was at the limits of its endurance flight envelope. Furthermore, at low altitudes when landing the fast 900 MHz got out of range, while the round time for the Iridium modem was about 3 s each way, putting extra strain on this fast decision making. On top of that, due to late development changes and the inability to test at the site because all systems had to be turned off while other competitors were flying, the video stream of the onboard images was inadvertently disabled. Then during the competition run, several strong whirlwinds were observed in the area, which led the operators to expect lateral deviations from the desired flight path. Last but not least, the landing area was surrounded by tall trees which were higher than the maximum reliable distance measurement range of the stereo camera.

All factors combined led to a chain of events where due to lack of expected visual information from the camera system and time pressure from the limited flight time, operators manually instructed the *DelftaCopter* to land at the location of the best visual detection instead of the properly predefined backup landing location. Since there had been no detection, the *DelftaCopter* started landing at its takeoff location, many kilometers away. While doing so it started moving toward a line of trees. The presence of whirlwinds and reduced situation awareness from the separated data links in different laptops delayed the insight that this was an active navigation action and not a temporary disturbance. Finally, the latency of the data link and operation at low altitudes due to headwinds with very high trees meant the operator noticed the problem of drifting toward trees seconds too late to abort the landing at a bad location in time. The *DelftaCopter* made a controlled landing

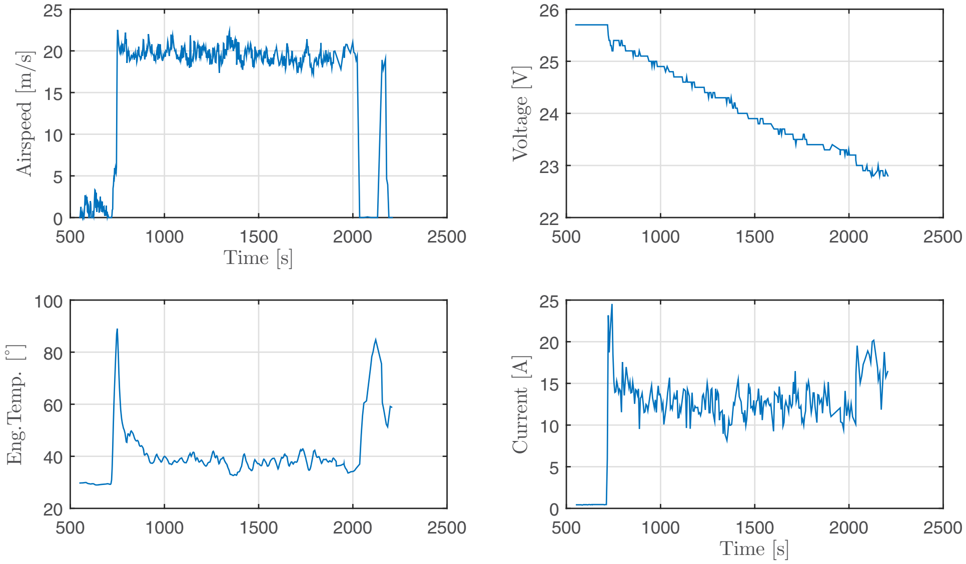

FIGURE 40 Competition flight data of the flight to Joe. The average airspeed during the flight was roughly 40 kt or 21.5 m/s. During hover,the engine temperature rises to 80° but during forward flight it settles at a value of about 40°. The current during the climbing hover in the first phase is about 23 A, 540 W. During the cruise the current reduces to about 12 A, 280 W. Nonclimbing hover is achieved at 18 A, 420 W

into a 23meter high Australian gum tree and was later recovered with only minor damage to the rotor blades.

11 | CONCLUSION

11.1 | Concept

The novel *DelftaCopter* concept was proposed with its efficient hovering with one large rotor, control authority in hover with fast cyclic control, simple and structurally strong biplane delta wing design that also serves as landing gear and yields improved stall behavior over single wings. The biplane also reduces the lateral surface affected by turbulence and wind during hover of this tail-sitter VTOL aircraft. While the swash plate adds mechanical complexity and maintenance, it yields very fast large control moments and is crucial to the efficiency of both hover and forward flight. The *DelftaCopter* was built, tested in a wind tunnel setup and in-flight. Finally, the *DelftaCopter* participated in the *Outback Medical Express Challenge 2016* where it won the second prize.[‖‖]

The concept is applicable to a variety if scenarios, especially when long-distance and efficient hovering at minimal weight are driving requirements.

11.2 | Propulsion

The hover efficiency of the *DelftaCopter* is high thanks to its large single low rpm optimized rotor. The energy efficiency during fast forward flight turned out to be lower than expected from computations. This is most likely due to higher than expected drag of the final airframe combined with significantly reduced motor efficiency at high torque.

11.3 | Control

The cyclic control of the *DelftaCopter* yields very fast and powerful attitude control. But without taking into account the rotor–fuselage dynamics, unacceptable couplings were observed. When designing hybrid aircraft that are mixing conventional cyclic controlled helicopters and fixed wings, it is crucial to understand the interactions between rotor and wing to optimize the design. The *Lock number* and rotor hinge spring stiffness K were shown to influence the speed of the rotor response. When adding a fuselage with high inertia to the model, it showed the same type of behavior in simulation as the real the *DelftaCopter*. The nonhomogeneous inertia of the fuselage and fuselage–rotor interactions adds nonsymmetrical couplings between the pitch and roll axes and affect the direction of the control effectiveness of the swash plate. Compensation for the above effects was derived and converted to a controller strategy to remove unwanted couplings sufficiently for flight.

11.4 | Vision

The stereo depth map properties of the S.L.A.M.dunk[***] allow path planning around obstacles and selection of flat areas during landing. But because of the very wide field-of-view fish-eye lenses, the resolution of the images when flying at cruise altitude is low. This makes reliable fully autonomous search for persons at a higher altitude very difficult. Still, the large field of view provided by the fish-eye lens meant the *DelftaCopter* could perform its mission with one fixed stereo camera, even though the aircraft tilts 90°. A salient detector with human feedback option was developed to automate the mission as much as possible while allowing human validation of the selected target. The *DelftaCopter* was also capable of autonomously selecting a safe landing

---

[‖‖] http://www.delftacopter.nl/

[***] S.L.A.M.dunk from https://www.parrot.com/

spot on the basis of texture analysis. During the landing phase, a fully autonomous obstacle avoidance algorithm ensured safe landing based on the depth map provided by stereo vision.

12 | RECOMMENDATIONS AND FUTURE WORK

The current design has shown outstanding efficiency in hovering flight and slightly less efficiency than predicted during forward flight. During the *Outback Medical Express Challenge* but also most other application scenarios of the *DelftaCopter*, the forward flight phase is the predominant mode of flight.

A future design could therefore place slightly less emphasis on hover efficiency and more on forward flight where some efficiency gains highly affect the operational range and flight speed. A smaller diameter rotor/propeller will also put less demand on the torque requirements of the direct drive motor which was currently overloaded in fast forward flight.

When higher torque direct drive brushless motors become available, they could also yield efficiency improvements in fast forward flight.

Although sufficient information about the flight dynamics was gathered in this work to allow successful flight, still many aspects could benefit from further research.

Showing the capabilities of the *DelftaCopter* in the presence of wind is a complex topic. To start with, there is the difference between maximum absolute wind and maximum turbulence. The former requires high maximum cruise speeds and the latter powerful fast moment and force generation. While it was shown that the *DelftaCopter* can take off and land with wind speeds up to 7 m/s, a more detailed comparison with other types of UAV would be desired.

Another topic is the interaction between the wing and the rotor. Especially the influence of wing forces on the rotor wwas not studied in detail for the forward flight. And while the simulation model did lead to a solution for initial flying of the platform, it is also clear that a lot of dynamics remains unmodeled. Small angle simplifications, simplified modeling and linear equations are expected to influence the results. Further insights could be gained from more detailed modeling, measuring different rotor weights,and measuring different fuselage inertia configurations. Future work will try to address these questions.

ACKNOWLEDGMENTS

We thank the sponsors of the TU-Delft Outback Medical Challenge Entry to have made this research possible.

ORCID

Christophe De Wagter http://orcid.org/0000-0002-6795-8454
Ewoud J. J. Smeur http://orcid.org/0000-0002-0060-6526
Kevin G. van Hecke http://orcid.org/0000-0001-9459-9592

REFERENCES

Anderson, J. D. (1999). *Aircraft performance & design*, volume 1. Boston, MA: WCB/McGraw-Hill Boston.

Anderson, S. B. (1981). Historical overview of v/stol aircraft technology. https://ntrs.nasa.gov/search.jsp?R=19810010574

Bapst, R., Ritz, R., Meier, L., & Pollefeys, M. (2015). Design and implementation of an unmanned tail-sitter. In *2015 IEEE/RSJ International Conference on Intelligent Robots and Systems (IROS)* (pp. 1885–1890). Piscataway, NJ: IEEE.

Boura, D., Hajicek, D., & Semke, W. (2011). Automated air drop system for search and rescue applications utilizing unmanned aircraft systems. In *Infotech@ Aerospace*, St. Louis, Missouri, Reston, VA, USA, AIAA (pp. 29–31). https://doi.org/10.2514/6.2011-1528

Bramwell, A. R., Balmford, D., & Done, G. (2001). *Bramwell's helicopter dynamics*. Oxford, England: Butterworth-Heinemann.

Brisset, P., Drouin, A., Gorraz, M., Huard, P.-S., & Tyler, J. (2006). The paparazzi solution. In *MAV 2006, 2nd US-European Competition and Workshop on Micro Air Vehicles*. Sandestin, United States. https://hal-enac.archives-ouvertes.fr/hal-01004157/

Çetinsoy, E., Dikyar, S., Hançer, C., Oner, K., Sirimoglu, E., Unel, M., & Aksit, M. (2012). Design and construction of a novel quad tilt-wing UAV. *Mechatronics*, 22(6), 723–745.

Clothier, R. A., Williams, B. P., & Fulton, N. L. (2015). Structuring the safety case for unmanned aircraft system operations in non-segregated airspace. *Safety Science*, 79, 213–228.

Cover, T., & Hart, P. (1967). Nearest neighbor pattern classification. *IEEE Transactions on Information Theory*, 13(1), 21–27.

De Oliveira, D. C., & Wehrmeister, M. A. (2016). Towards real-time people recognition on aerial imagery using convolutional neural networks. In *2016 IEEE 19th International Symposium on Real-Time Distributed Computing (ISORC)* (pp. 27–34). Piscataway, NJ: IEEE.

De Wagter, C., Dokter, D., de Croon, G., & Remes, B. (2013). Multi-lifting-device UAV autonomous flight at any transition percentage. Paper presented at *European Guidance Navigation and Control Conference*. CEAS.

De Wagter, C., & Smeur, E. (2016). Control of a hybrid helicopter with wings. *Journal of Micro Air Vehicles*, 9(3), 209–217. https://doi.org/10.1177/1756829317702674

Drela, M., Youngren, H., Scherrer, M., & Deperrois, A. (2012). Xflr-5. http://www.xflr5.com

Erdos, D., Erdos, A., & Watkins, S. E. (2013). An experimental UAV system for search and rescue challenge. *IEEE Aerospace and Electronic Systems Magazine*, 28(5), 32–37.

Erdos, D., & Watkins, S. E. (2008). UAV autopilot integration and testing. In *2008 IEEE Region 5 Conference* (pp. 1–6). Piscataway, NJ: IEEE.

Escareno, J., Sanchez, A., Garcia, O., & Lozano, R. (2008). Modeling and global control of the longitudinal dynamics of a coaxial convertible mini-UAV in hover mode. In *Unmanned Aircraft Systems* (pp. 261–273). Berlin, Germany: Springer.

Escareno, J., Stone, R., Sanchez, A., & Lozano, R. (2007). Modeling and control strategy for the transition of a convertible tail-sitter UAV. In *2007 European Control Conference (ECC)* (pp. 3385–3390). Piscataway, NJ: IEEE.

Fresk, E., & Nikolakopoulos, G. (2013). Full quaternion based attitude control for a quadrotor. In *European Control Conference* (pp. 3864–3869). Piscataway, NJ: IEEE.

Gaszczak, A., Breckon, T. P., & Han, J. (2011). Real-time people and vehicle detection from UAV imagery. In *IS&T/SPIE Electronic Imaging (article 78780B)*. Bellingham WA: International Society for Optics and Photonics.

Gati, B. (2013). Open source autopilot for academic research-the paparazzi system. In *American Control Conference (ACC), 2013* (pp. 1478–1481). Piscataway, NJ: IEEE.

Gavrilets, V. (2015). Dynamic model for a miniature aerobatic helicopter. In *Handbook of unmanned aerial vehicles* (pp. 279–306). Berlin, Germany: Springer.

Glauert, H. (1935). Airplane propellers. In *Aerodynamic theory* pp. 169–360). Berlin, Germany: Springer.

Hulsman, S., De Groot, J., & Dokter, D. (2014). Atmos UAV: High-tech startup with game-changing ideas. *Leonardo Times*, 18(1), 2014.

Itasse, M., Moschetta, J.-M., Ameho, Y., & Carr, R. (2011a). Equilibrium transition study for a hybrid mav. *International Journal of Micro Air Vehicles*, 3(4), 229–245.

Itasse, M., Moschetta, J.-M., Carr, R., & Ameho, Y. (2011b). Equilibrium transition study for a hybrid mav. In de Croon, G. and Amelink, M., (Eds.), *Proceedings of the International Micro Air Vehicle Conference and Flight Competition 2011*, 't Harde, the Netherlands, IMAV, (summer edition, pp. 79–86). https://doi.org/10.4233/uuid:eadf2fe7-7e5a-4cf8-88e5-6c247f5b6fa9

Johnson, W. (1980). A comprehensive analytical model of rotorcraft aerodynamics and dynamics. part 1. analysis development. Technical report, NASA Ames Research Center, DTIC Document.

Ke, Y., Wang, K., & Chen, B. M. (2016). A preliminary modeling and control framework for a hybrid UAV j-lion. In P. Z. Peng and D. F. Lin (Eds.), *International Micro Air Vehicle Competition and Conference 2016* (pp. 28–34). Beijing, People's Republic of China, IMAV.

Knoebel, N. B., & McLain, T. W. (2008). Adaptive quaternion control of a miniature tailsitter UAV. In *American Control Conference, 2008* (pp. 2340–2345). Piscataway, NJ: IEEE.

Larminie, J., Dicks, A., & McDonald, M. S. (2003). *Fuel cell systems explained*, volume 2. Chichester, England: Wiley.

Matsumoto, T., Kita, K., Suzuki, R., Oosedo, A., Go, K., Hoshino, Y., Konno, A., & Uchiyama, M. (2010). A hovering control strategy for a tail-sitter VTOL UAV that increases stability against large disturbance. In *2010 IEEE International Conference on Robotics and Automation (ICRA)* (pp. 54–59). Piscataway, NJ: IEEE.

Olson, E. C., & Selberg, B. (1976). Experimental determination of improved aerodynamic characteristics utilizing biplane wing configurations. *Journal of Aircraft*, 13(4), 256–261.

Oosedo, A., Abiko, S., Konno, A., Koizumi, T., Furui, T., & Uchiyama, M. (2013). Development of a quad rotor tail-sitter VTOL UAV without control surfaces and experimental verification. In *2013 IEEE International Conference on Robotics and Automation (ICRA)* (pp. 317–322). Piscataway, NJ: IEEE.

Padfield, G. D. (2008). *Helicopter flight dynamics*. Hoboken, NJ: Wiley.

Phung, D.-K., & Morin, P. (2013). Modeling and energy evaluation of small convertible UAVS. *IFAC Proceedings Volumes*, 46(30), 212–219.

Prouty, R. W. (1995). *Helicopter performance, stability, & control*. Melbourne, FL: Krieger.

Rosenstein, H., & Clark, R. (1986). Aerodynamic development of the v-22 tilt rotor. Paper presented at *Twelfth European Rotorcraft Forum*.

Roskam, J., & Lan, C.-T. E. (1997). *Airplane aerodynamics and performance*. Lawrence, KS, USA, DARcorporation.

Rudol, P., & Doherty, P. (2008). Human body detection and geolocalization for UAV search and rescue missions using color and thermal imagery. In *2008 IEEE Aerospace Conference* (pp. 1–8). Piscataway, NJ: IEEE.

Schenk, H. (2007). PropCalc- propeller calculator software. Retrieved from http://www.drivecalc.de/PropCalc/.

Schütt, M., Hartmann, P., & Moormann, D. (2014). Fullscale windtunnel investigation of actuator effectiveness during stationary flight within the entire flight envelope of a tiltwing mav. In G. de Croon, E. van Kampen, C. D. Wagter, & C. de Visser (Eds.), *International Micro Air Vehicle Competition and Conference 2014*, Delft, The Netherlands, IMAV (pp. 77–83).

Shim, H., Koo, T. J., Hoffmann, F., & Sastry, S. (1998). A comprehensive study of control design for an autonomous helicopter. In *Proceedings of 37th IEEE Conference on Decision and Control* (pp. 1–6). Piscataway, NJ: IEEE.

Smeur, E., Chu, Q., de Croon, G., Remes, B., Wagter, C. D., & van der Horst, E. (2014). Modelling of a hybrid UAV using test flight data. In G. de Croon, E. van Kampen, C. D. Wagter, & C. de Visser (Eds.), *International Micro Air Vehicle Competition and Conference 2014*, IMAV, Delft, The Netherlands. (pp. 196–203).

Smeur, E., de Croon, G. & Chu, Q. (2016). Gust disturbance alleviation with incremental nonlinear dynamic inversion. In *International Conference on Intelligent Robots and Systems (IROS)*, pp. 5626–5631. IEEE/RSJ.

Stepniewski, W. Z., & Keys, C. (1979). *Rotary-wing aerodynamics*. Massachusetts, USA, Courier Corporation.

Thornthwaite, C., & Kaser, P. (1943). Wind-gradient observations. *Eos, Transactions American Geophysical Union*, 24(1), 166–182.

UAVChallenge (2016). Uav challenge medical express competition rules 2016 v4. Retrieved from https://drive.google.com/open?id=0B5JgqjkRDqw8TjEwUVdmVV94ZkE.

Verling, S., Weibel, B., Boosfeld, M., Alexis, K., Burri, M., & Siegwart, R. (2016). Full attitude control of a VTOL tailsitter UAV. In *2016 IEEE International Conference on Robotics and Automation (ICRA)* (pp. 3006–3012). Piscataway, NJ: IEEE.

Wagtendonk, W. J. (1996). *Principles of helicopter flight*. Newcastle, WA: Aviation Supplies & Academics.

Wong, K., Guerrero, J. A., Lara, D., & Lozano, R. (2007). Attitude stabilization in hover flight of a mini tail-sitter UAV with variable pitch propeller. In *2007 IEEE/RSJ International Conference on Intelligent Robots and Systems* (pp. 2642–2647). Piscataway, NJ: IEEE.

How to cite this article: De Wagter C, Ruijsink R, Smeur EJ, et al. Design, control, and visual navigation of the *DelftaCopter* VTOL tail-sitter UAV. *J Field Robotics*. 2018;35: 937–960. https://doi.org/10.1002/rob.21789

APPENDIX A

Figure A1 shows the three views of the *DelftaCopter* with sizing information. Key specification values of the *DelftaCopter* are repeated in Table AI. Finally Figure A2 gives an overview of the team.

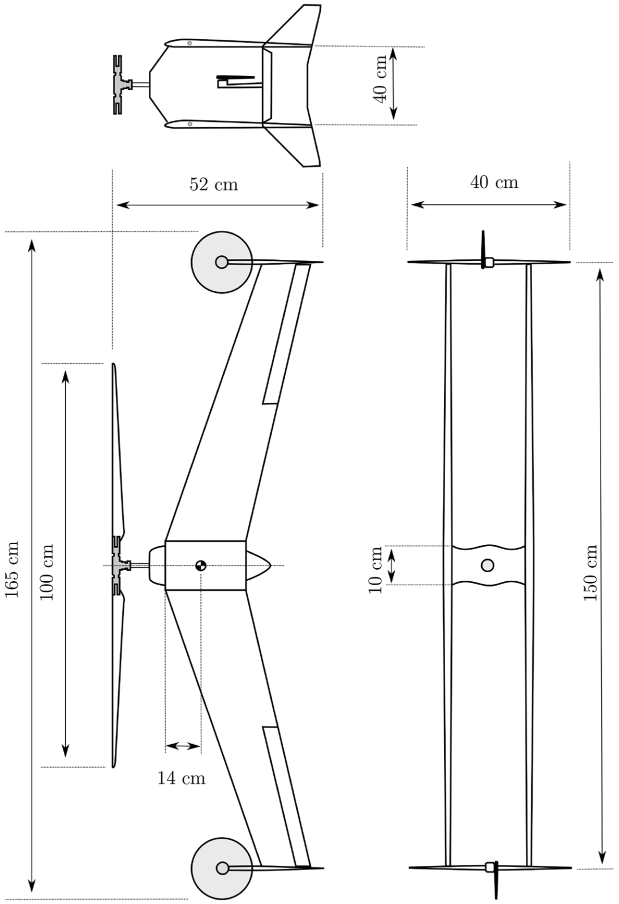

FIGURE A1 Plan view of the *DelftaCopter*. The center part consists of a 480-sized helicopter head with a direct drive motor. Two pairs of delta wings form a box structure. The wing tips are stabilizing the delta wing by increasing its C_{m_β}, they connect the top and bottom wing and provide structural strength while housing modems and acting as landing gear

TABLE AI *DelftaCopter* key specifications

Property	Value
Weight	4.3 kg
MTOW	4.5 kg
Wing area	0.496 m^2
Wing loading	8.7 kg/m^2
Span	1.54 m
Length	0.6 m
Height	0.4 m
Design cruise speed	20.5 m/s (40 kt)
Measured cruise speed	19.5 m/s to 20 at 4.3 kg
Measured cruise power	300 W at 4.3 kg 20 m/s
Theoretical most efficient speed	18.0 m/s (35 kt)
Measured power at most efficient speed	280 W at 18.0 m/s
Theoretical maximum speed	25.5 m/s (49.5 kt)
Measured maximum speed	23.5 m/s
Measured hover power (4.3 kg)	420 W at 1650 rpm
Measured climb power (4.3 kg)	600 W at 1650 rpm
Main battery	10.5 Ah 6 Cell LiPo
FTD battery	250 mAh 2 Cell LiFe

FTD, flight termination device; MTOW, maximum take of weight.

FIGURE A2 *DelftaCopter* team at the *Outback Medical Express UAV Challenge 2016*, Dalby Australia